# A Modeling Study of Global Distribution and Formation Pathways of Highly Oxygenated Organic Molecules (HOMs) from Monoterpenes

Xinyue Shao[1,2], Yaman Liu[1,3], Xinyi Dong[1,2], Minghuai Wang[1,2], Ruochong Xu[4,5], Joel A. Thornton[5], Duseong S. Jo[6], Man Yue[3], Wenxiang Shen[1,2], Manish Shrivastava[7], Stephen R. Arnold[8], and Ken S. Carslaw[8]

[1]School of Atmospheric Science, Nanjing University, Nanjing, China
[2]Joint International Research Laboratory of Atmospheric and Earth System Sciences & Institute for Climate and Global Change Research, Nanjing University, China
[3]Zhejiang Institute of Meteorological Sciences, Hangzhou, China
[4]Department of Earth System Science, Ministry of Education Key Laboratory for Earth System Modeling, Institute for Global Change Studies, Tsinghua University, Beijing, China
[5]Department of Atmospheric Sciences, University of Washington, Seattle, WA, USA
[6]Department of Earth Science Education, Seoul National University, Seoul, 08826, South Korea
[7]Pacific Northwest National Laboratory, Richland, Washington, USA
[8]School of Earth and Environment, University of Leeds, Leeds, LS2 9JT, UK

*Correspondence to*: Xinyi Dong (dongxy@nju.edu.cn), Minghuai Wang (minghuai.wang@nju.edu.cn)

**Abstract.** Highly oxygenated organic molecules (HOMs) derived from monoterpenes are key precursors of secondary organic aerosols (SOA), yet their global-scale formation pathways and climate impacts remain poorly quantified due to uncertainties in autoxidation kinetics and branching ratios of peroxy radicals. Here, we integrate a comprehensive HOMs chemical mechanism into a global climate model, enabling a systematic evaluation of HOMs-derived SOA (HOMs-SOA) contributions and their sensitivity to key chemical parameters. The improved model shows reasonable agreement in the diurnal cycle and average HOM concentrations (normalized mean biases of 69% and 121% at the two sites). Sensitivity experiments identify the branching ratio of autoxidation-capable peroxy radicals (MT-b$RO_2$) as the dominant uncertainty source. While the MT-b$RO_2$ branching ratio has limited impact on $C_{10}$-HOMs concentrations (~60% formed via NO-terminated autoxidation), it strongly regulates $C_{15}$/$C_{20}$-HOM concentrations produced through cross-reactions of biogenic peroxy radicals. The contribution of HOMs-SOA to total monoterpene-derived SOA ranges from 19% to 41%, depending on the MT-b$RO_2$ branching ratio used in chamber experiments. $C_{15}$ and $C_{20}$ accretion products dominate in pristine regions (e.g., the Amazon, contributing ~50% of HOMs-SOA), whereas anthropogenic-influenced areas (e.g., southeastern China and India) exhibit higher contributions from NO-mediated formation of $C_{10}$-ON (nitrate HOMs). Our findings advance the representation of organic aerosols in climate models and provide critical insights to bridge gaps between chamber experiments and global-scale simulations.

## 1 Introduction

Monoterpenes are one of the most significant classes of biogenic volatile organic compounds (BVOCs) (Guenther et al., 2012). Monoterpene-derived organic peroxy radicals (MT-$RO_2$) can undergo complex photochemical oxidation processes in the atmosphere. These processes can rapidly generate extremely low-volatility organic compounds (ELVOCs) through intramolecular autoxidation reactions that involve hydrogen-atom shifts and molecular oxygen attachment to form peroxy radicals (Ehn et al., 2014; Crounse et al., 2013; Praske et al., 2018; Bianchi et al., 2019). ~~As the number of oxygen atoms in the functional group increases, the volatility of the organics gradually decreases.~~ Organic compounds generated through rapid autoxidation reactions that contain six or more oxygen atoms are referred to as highly oxygenated organic molecules (HOMs), and can contribute to secondary organic aerosols (SOA) formation (Bianchi et al., 2019). The SOA formed by HOMs are referred to as HOMs-SOA.

Studies have shown that monoterpene-derived HOMs promote new particle formation (NPF) due to their low volatility, affecting the concentrations of the cloud condensation nuclei (CCN), ultimately influencing radiative forcing. Ehn et al. (2014) found that HOMs made important contributions to the growth of particles with diameters between 5 and 50 nm in northern forests. Jokinen et al. (2015) combined chamber experiments with global model simulations and found that monoterpene-derived HOMs promote NPF in continental regions, especially under high supersaturation conditions, thereby increasing CCN concentrations. HOMs account for 27~47% of SOA produced from oxygenated monoterpenes emitted by sage plants in California (Mehra et al., 2020). Airborne measurements above the Finnish boreal forest indicated that HOMs are distributed at the top of the boundary layer during the daytime (Beck et al., 2022). Moreover, a regional model also demonstrated that HOMs dominated the NPF at an altitude of 13 km in the Amazon region where human activities have less impact, significantly contributing to CCN formation (Zhao et al., 2020). Accordingly, Gordon et al. (2016) found through global model simulations that new particles formed by monoterpene-derived HOMs result in a 27% reduction in radiative forcing from -0.28 $W/m^2$ to -0.06 $W/m^2$ due to cloud albedo variation from the preindustrial to the present condition. Similarly, Zhu et al. (2019) found that simulated new particles formed by monoterpene-derived HOMs reduced direct and indirect radiative forcing by 12.5% since the Industrial Revolution.

Despite these past studies, the formation mechanism of monoterpene-derived HOMs remains uncertain in several aspects, including the reaction rate, yields of reactions (including autoxidation reactions, self-reactions and cross-reactions), and the impact of nitrogen ~~di~~oxide<u>s</u> ($NO_x$) on their generation process. Monoterpenes are emitted into the atmosphere and rapidly oxidized by OH radicals or $O_3$ to generate peroxy radicals ($RO_2$), but the proportion of $RO_2$ radicals that can further undergo autoxidation reactions is not yet clear (Berndt et al., 2016; Kurten et al., 2015; Richters et al., 2016; Roldin et al., 2019). In addition, the reaction rates of autoxidation reactions remain highly uncertain, with different measurements in different chamber experiments ranging from 0.6 to 21 /s, differing by 1 to 2 orders of magnitude (Lee et al., 2023; Berndt et al., 2016; Moller et al., 2020). After autoxidation reactions, $RO_2$ radicals can undergo self-reactions and cross-reactions, generating accretion

products with more carbon atoms and lower volatility. The yields and reaction rates ~~of the~~ to form accretion products also vary by one to two orders of magnitude in different experimental measurements (Berndt et al., 2018; Zhao et al., 2018; Roldin et al., 2019; Baker et al., 2024; Zhao et al., 2017; Molteni et al., 2019), with reported values ranging from $5 \times 10^{-12}$ cm$^3$ s$^{-1}$ (Baker et al., 2024) to $1 \times 10^{-10}$ cm$^3$ s$^{-1}$ (Berndt et al., 2018). Moreover, $NO_x$ has a dual effect on HOMs formation. On the one hand, $NO_x$ can promote HOMs formation by enhancing atmospheric oxidation and promoting alkoxyl radicals and subsequent $RO_2$ radicals, or even organic nitrate formation. On the other hand, $NO_x$ can terminate multi-generational oxidation reactions that generate HOMs. Nevertheless, due to insufficient experimental data, modeling calculations are needed to constrain the reaction kinetic parameters of these uncertain processes.

Several modeling studies have been conducted to simulate HOMs formation, and most of them focus on theoretical simulation. Pye et al. (2019) represented the chemical formation reactions of HOMs through the yield of important organic peroxy radicals from chamber experiments. Roldin et al. (2019) developed a one-dimensional column model with a near-explicit mechanism of HOMs, though it has not been applied on a global scale. Weber et al. (2021) and Xu et al. (2022) developed and summarized these explicit formation mechanisms of monoterpenes-derived HOMs in global models but the models still lack ~~fully understand~~ a full understanding of the uncertainties. Recently, Zhao et al. (2024) advanced global modeling capabilities by comprehensively integrating 11 NPF mechanisms, revealing the critical role of organic-driven pathways in aerosol formation across diverse regions.

In this study, the Community Atmosphere Model version 6 with comprehensive tropospheric and stratospheric chemistry (CAM6-Chem) has been revised with the chemical mechanism and gas-particle partitioning processes of HOMs, aiming to better understand their formation and spatiotemporal distribution. Section 2 introduces the model with the revised mechanism of HOMs and sensitivity experiments used in this study. Section 3 validates the revised model with field campaigns, demonstrates the spatiotemporal characteristics of HOMs, explores the dominant formation pathways of HOMs, and discusses the uncertainties in HOM chemistry. Results are summarized and discussed in Section 4.

## 2 Data and methods

### 2.1 Model configuration

The Community Atmosphere Model version 6 with comprehensive tropospheric and stratospheric chemistry (CAM6-Chem) from the Community Earth System Model version 2.1.0 (CESM2.1.0) is used in this study (Danabasoglu et al., 2020). The default configuration of CAM6-Chem employs the four-mode version of the Modal Aerosol Module (MAM4) (Liu et al., 2016) and applies the Volatility Basis Set (VBS) approach (Donahue et al., 2006; Hodzic et al., 2016; Jo et al., 2021; Robinson et al., 2007) to represent the formation of SOA from all volatile organic compounds (VOCs). All simulations are configured with a horizontal resolution of 0.95° in latitude and 1.25° in longitude and a vertical resolution of 32 layers up to approximately 40 km (Emmons et al., 2020). Meteorological fields, including temperature, winds, and surface fluxes, from the Modern-Era

Retrospective analysis for Research and Applications (MERRA2) reanalysis data set (Gelaro et al., 2017) are used for offline nudging to minimize uncertainties in meteorology simulation (Jo et al., 2021; Tilmes et al., 2019; Liu et al., 2021). Anthropogenic and biomass burning emissions are from the standard Coupled Model Intercomparison Project 6 (CMIP6) (Eyring et al., 2016). The biogenic emissions are simulated online using the Model of Emissions of Gases and Aerosol from Nature version2.1 (MEGAN2.1) (Guenther et al., 2012).

The simulation period spanned from June to July 2013 and from April to June 2014, corresponding to the field campaign periods (SENEX and BAECC, see Section 2.3), and was used to evaluate model improvements (with one month for spin-up). Additionally, to assess the contribution of different chemical reaction pathways in the formation of HOMs and the spatiotemporal distribution of HOMs-SOA, we conducted one-year simulations for 2013 (with one month for spin-up) across different sensitivity experiments (see Section 2.4).

This study uses an updated version of the model to better represent the heterogeneous production and photolytic depletion of SOA (Liu et al., 2023). One update involves coupling the model with the Model for Simulating Aerosol Interactions and Chemistry (MOSAIC) (Zaveri et al., 2021), enabling explicit representation of the heterogeneous uptake of IEPOX onto sulfate aerosols (Jo et al., 2019; Jo et al., 2021). Another update is the incorporation of a faster photolysis rate for monoterpene-derived SOA (MTSOA) according to recent chamber measurements (Epstein et al., 2010; Zawadowicz et al., 2020; Henry and Donahue, 2012) and modeling studies (Liu et al., 2021; Liu et al., 2023). A modest photolysis rate of MTSOA (2.0% of the $NO_2$ photolysis frequency) replaces the original rate (0.04% of the $NO_2$ photolysis frequency) in the default CAM6-Chem model (Hodzic et al., 2016), despite evidence suggesting that some MTSOA may resist degradation (Zawadowicz et al., 2020). Except for MTSOA, the photolysis rates of other SOA are unchanged (kept at 0.04% of $NO_2$ photolysis frequency) in the simulations due to a lack of chamber reports. HOM chemistry is also incorporated, including autoxidation reactions and self- and cross-reactions ~~for accretion products~~ of biogenic peroxy radicals forming accretion products, as described in Section 2.2.2.

## 2.2 HOMs formation mechanisms

### 2.2.1 Extension of volatility basis set (VBS)

SOA ~~are formed when emitted volatile organic compounds (VOCs) are oxidized in the atmosphere with subsequent gas-particle partitioning processes or new particle formation~~ are generated when volatile organic compounds (VOCs) undergo oxidation, leading to the formation of low-volatility gases that subsequently condense onto pre-existing aerosols. However, the physical and chemical properties of SOA are complicated due to the variety of VOCs, oxidants, and formation mechanisms. To simplify and represent the formation processes in the models, SOA and their gas-phase precursors (SOAG) are lumped based on their volatilities, following the volatility basis set (VBS) approach (Donahue et al., 2006; Robinson et al., 2007; Shrivastava et al., 2015). In CAM6-Chem, the volatilities of SOA and SOAG are categorized into five bins based on their

saturation concentrations (C*) of 0.01, 0.1, 1.0, 10.0, and 100.0 μg/m$^3$ at 298 K as shown in Table 1. The yield of SOAG from various VOCs, including isoprene, glyoxal, monoterpenes (α-pinene, β-pinene, limonene, and myrcene), the β-caryophyllene surrogate sesquiterpene, benzene, toluene, lumped xylenes, intermediate VOC (IVOC), and semi-VOC (SVOC), are based on Tilmes et al. (2019) and Jo et al. (2021) and shown in Table S10. The SOAG in different volatility bin (SOAG0~4 in Table 1) condenses on the preexisting aerosols to form SOA (soa1~5 in Table 1) based on their saturation vapor pressure calculated following Eq. (1) (Chung and Seinfeld, 2002):

$$P_{0,i}(T) = P_{0,i}(T_0) \cdot e^{\left[\frac{-\Delta H_{vap}}{R}\cdot\left(\frac{1}{T}-\frac{1}{T_0}\right)\right]} \quad (1)$$

where $P_{0,i}(T)$ is the saturation vapor pressure at temperature T and $T_0$=298 K; R is the ideal gas constant, and $\Delta H_{vap}$ is the enthalpies of vaporization which represents the energy to transform the liquid substance into gas phase (default parameterized values shown in Table 1).

For SOA species i and aerosol mode m, the equilibrium gas concentration is expressed as:

$$g_i^* = \frac{g_{0,i}}{M_{OA}} \times A_i \quad (2)$$

$g_{0,i}$ is the equilibrium gas mixing ratio derived from the saturation vapor pressure (Eq. (1) and specifically shown in Eq. (3)), $A_i$ is the particle-phase concentration of species i, and $M_{OA}$ is the total absorbing organic mass (including SOA and oxidized POA).

$$g_{0,i} = \frac{P_{0,i}(T)}{P} \quad (3)$$

where P is the atmospheric pressure.

The dynamic exchange between gas and particle phases is described by a first-order mass transfer equation:

$$\frac{dA_i}{dt} = (G_i - g_i^*) \times k_i \quad (4)$$

where $G_i$ is the gas-phase concentration and $k_i$ is the transfer coefficient. This formulation ensures mass conservation and is solved using a semi-implicit numerical scheme. Similar approaches are widely used in global climate models to represent SOA gas–particle partitioning within the volatility basis set (VBS) framework (Pankow, 1994; Donahue et al., 2006; Tilmes et al., 2015).

The volatility bins of the default VBS scheme are too high to represent the formation processes of HOMs. The volatilities of most HOMs fall within the range of low volatility organic compounds (LVOCs) and extremely low-volatility organic compounds (ELVOCs) (Bianchi et al., 2019). Therefore, the original five volatility bins ($C^*$ = 0.01, 0.1, 1.0, 10.0, and 100.0 μg/m$^3$) are extended to eight bins, with the newly added bins ($C^*$ = 1.0e-3, 1.0e-5, 1.0e-9 μg/m$^3$) explicitly representing the final products of HOMs chemistry (Table 2). The volatilities of these newly added HOMs are calculated based on their molecular formula (Table S11) using Eq. (2) (Mohr et al., 2019).

$$\log_{10}C^*(300\ \mathrm{K}) = (25 - n_C) \times b_C - (n_o - 3n_N) \times b_O - n_N \times b_N - 2\left[\frac{(n_o - 3n_N) \times n_C}{n_C + n_o - 3n_N}\right] \times b_{CO} \quad (5)$$

where $n_C$, $n_O$, and $n_N$ are the number of carbon, oxygen, and nitrogen atoms; $b_C$ = 0.475; $b_O$ = 0.2; $b_N$ = 2.5; $b_{CO}$ = 0.9.

**Table 1.** The saturated vapor concentration (C*) and vaporization enthalpies ($\Delta H_{vap}$) of SOAG (SOA precursor gas) at the traditional VBS bins.

| $C^*$ (μg/m$^3$) | SOAG | $\Delta H_{vap}$ (kJ/mol) |
|---|---|---|
| 1.0 x 10$^{-2}$ | SOAG0 | 153.0 |
| 1.0 x 10$^{-1}$ | SOAG1 | 142.0 |
| 1.0 | SOAG2 | 131.0 |
| 1.0 x 10 | SOAG3 | 120.0 |
| 1.0 x 10$^2$ | SOAG4 | 109.0 |

**Table 2**. The saturated vapor concentration (C*) and vaporization enthalpies ($\Delta H_{vap}$) of HOMs.

| $C^*$ (μg/m$^3$) | $\Delta H_{vap}$ (kJ/mol) | Short Name |
|---|---|---|
| 1.0 x 10$^{-3}$ | 164.0 | $C_{10}$-aNON |
| | | $C_{10}$-bNON |
| | | $C_{10}$-ON |
| 1.0 x 10$^{-5}$ | 186.0 | $C_{15}$ |
| 1.0 x 10$^{-9}$ | 230.0 | $C_{20}$ |

### 2.2.2 Autoxidation

To account for the H-shift chemistry of MT-$RO_2$ leading to HOM formation (i.e., autoxidation), the first-generation monoterpene-derived $RO_2$ (MT-$RO_2$), formed via reactions of monoterpenes (MT) with OH or $O_3$, is classified into two categories: MT-a$RO_2$ and MT-b$RO_2$ (Fig. 1). Both categories undergo standard bimolecular reactions, but only MT-b$RO_2$ species proceed through autoxidation. In contrast, MT-a$RO_2$ species (such as $APINO_2$, $BPINO_2$, $LIMONO_2$, and $MYRCO_2$, listed in Table S11) do not participate in autoxidation.

Relatively high branching ratios for the formation of MT-b$RO_2$ are adopted, based on the values used in Table S3 of Xu et al. (2022). Specifically, the branching ratio of MT-b$RO_2$ is 0.75 for monoterpene + OH reactions, and 0.08 for monoterpene + $O_3$ reactions (Fig. 1). These values fall within the ranges reported in previous studies. Literature-based yields for MT-b$RO_2$ range from 0.075 to 0.83 for OH-initiated reactions (Lee et al., 2023; Piletic and Kleindienst, 2022; Pye et al., 2019; Weber et al., 2020; Xu et al., 2019) and from 0 to 0.22 for $O_3$-initiated reactions (Ehn et al., 2014; Jokinen et al., 2015; Roldin et al., 2019; Berndt et al., 2016; Kurtén et al., 2015; Richters et al., 2016). The reaction rate constants for OH and $O_3$ oxidation of monoterpenes are the same as those used in the default mechanism (Table 3), and apply equally to the formation of both MT-a$RO_2$ and MT-b$RO_2$. This approach is fully consistent with the implementation in GEOS-Chem by Xu et al. (2022), who demonstrated that such simplification can reasonably reproduce the formation of HOMs and the fate of $RO_2$ radicals. Furthermore, studies by Roldin et al. (2019) and Weber et al. (2020) confirmed that using the same reaction rate for MT-b$RO_2$ and MT-a$RO_2$ also yields HOM concentrations that agree well with observations under forested conditions.

MT-b$RO_2$ are assumed to undergo one or multiple generations of autoxidation (Table 4). These reactions follow a temperature-dependent rate with an activation energy of 74.1 kJ/mol, consistent with previous studies (Lee et al., 2023; Pye et al., 2019; Roldin et al., 2019; Schervish and Donahue, 2020; Xu et al., 2019). The corresponding autoxidation rate are 0.27 $s^{-1}$ at 283 K, 1.30 $s^{-1}$ at 298 K, and 4.12 $s^{-1}$ at 310 K. The yield of HOMs depends on both the autoxidation rate and the fraction of MT-$RO_2$ that undergoes autoxidation. To reflect the uncertainty associated with these parameters, this fraction is varied in both OH- and $O_3$-initiated pathways as part of sensitivity experiments. A detailed discussion of these tests is provided in Section 2.3.

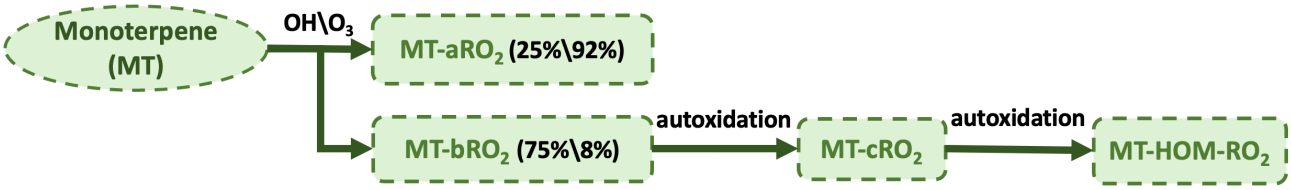


**Figure 1.** Schematic of monoterpene (MT) oxidation and subsequent autoxidation pathways. MT reacts with OH or $O_3$ to form MT-aRO$_2$ or MT-bRO$_2$, with the latter undergoing autoxidation steps to yield HOMs. Branching ratios are shown for OH and $O_3$ pathways.

**Table 3.** Initial oxidation reactions of four representative monoterpenes (APIN, BPIN, LIMON, and MYRC) with OH and $O_3$, leading to the formation of MT-aRO$_2$ (non-autoxidizable) and MT-bRO$_2$ (autoxidizable). Detailed descriptions of the intermediate species are provided in Table S11.

| Index | Reactions | Reaction rate |
|---|---|---|
| 1 | APIN[a] + OH → 0.25*MT-aRO$_2$ + 0.75*MT-bRO$_2$ | 1.34e-11*exp(410/T) |
| 2 | BPIN[a] + OH → 0.25*MT-aRO$_2$ + 0.75*MT-bRO$_2$ | 1.62e-11*exp(460/T) |
| 3 | LIMON[a] + OH → 0.25*MT-aRO$_2$ + 0.75*MT-bRO$_2$ | 3.41e-11*exp(470/T) |
| 4 | MYRC[a] + OH → 0.25*MT-aRO$_2$ + 0.75*MT-bRO$_2$ | 2.1e-10 |
| 5 | APIN[a] + $O_3$ → 0.736*MT-aRO$_2$ + 0.064*MT-bRO$_2$ + 0.77*OH + 0.066*TERPA2$O_2$ + 0.22*$H_2O_2$ + 0.044*TERPA + 0.002*TERPACID + 0.034*TERPA2 + 0.17*$HO_2$ + 0.17*CO + 0.27*$CH_2O$ + 0.054*TERPA2$CO_3$ | 1.34e-11*exp(410/T) |
| 6 | BPIN[a] + $O_3$ → 0.736*MT-aRO$_2$ + 0.064*MT-bRO$_2$ + 0.102*TERPK + 0.3*OH + 0.06*TERPA2$CO_3$ + 0.32*$H_2O_2$ + 0.038*BIGALK + 0.19*$CO_2$ + 0.81*$CH_2O$ + 0.11*HMHP + 0.08*HCOOH | 1.62e-11* exp(460/T) |
| 7 | LIMON[a] + $O_3$ → 0.736*MT-aRO$_2$ + 0.064*MT-bRO$_2$ + 0.66*OH + 0.132*TERPF1 + 0.33*$CH_3CO_3$ + 0.33*$CH_2O$ + 0.066*TERPA3$CO_3$ + 0.33*$H_2O_2$ + 0.002*TERPACID | 3.41e-11*exp(470/T) |
| 8 | MYRC[a] + $O_3$ → 0.736*MT-aRO$_2$ + 0.064*MT-bRO$_2$ + 0.2*TERPF2 + 0.63*OH + 0.63*$HO_2$ + 0.25*$CH_3COCH_3$ +0.39*$CH_2O$ + 0.18*HYAC | 2.1e-10 |

[a] APIN, BPIN, LIMON, and MYRC represent α-pinene, β-pinene, limonene, and myrcene, respectively.

**Table 4.** Autoxidation reactions of MT-bRO$_2$ leading to the formation of MT-cRO$_2$ and subsequently MT-HOM-RO$_2$.

| Index | Reactions | Reaction rate |
|---|---|---|
| 9 | MT-bRO$_2$ → MT-cRO$_2$ | 9.8e12*exp(-8836/T) |
| 10 | MT-cRO$_2$ → MT-HOM-RO$_2$ | |

### 2.2.3 Self-Reactions and Cross-Reactions

Due to isomers of MT-RO$_2$ and ISOP-RO$_2$, self- and cross-reactions are included (Table 5), with three branches considered for the products. First, intermediate products are produced and are lumped as C$_{10}$-ROH and C$_{10}$-CBYL. Second, RO radicals are generated, which may produce HO$_2$ and C$_{10}$-CBYL or decompose into smaller compounds. Half of the RO radicals are assumed to decompose into smaller carbonyls. Third, accretion products (C$_{15}$ and C$_{20}$) are produced. The branching ratios of the three pathways above are set as 0.29:0.67:0.04, respectively (Xu et al., 2022). However, for the self- and cross-reactions involving MT-aRO$_2$ (APINO$_2$, BPINO$_2$, LIMONO$_2$, and MYRCO$_2$ in Table S11) and ISOP-RO$_2$, a small fraction of RO radicals may undergo a unimolecular H-shift to form MT-bRO$_2$, with the branching ratio set to 0.05 (Xu et al., 2022). The fast reaction rate is applied here based on Table S4 in Xu et al. (2022).

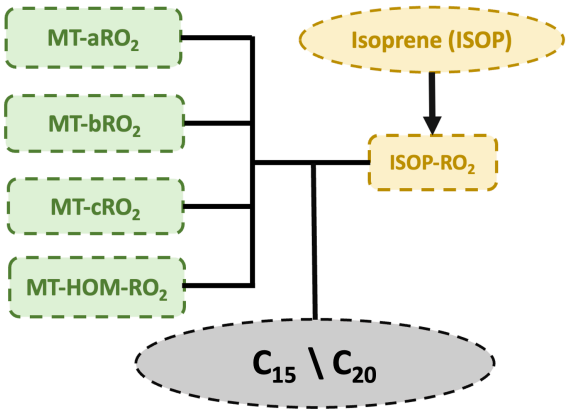


**Figure 2.** Schematic illustration of self- and cross-reactions between MT-RO$_2$ and ISOP-RO$_2$ peroxy radicals.

**Table 5.** Summary of the self- and cross-reactions involving MT-RO$_2$ and ISOP-RO$_2$ peroxy radicals considered in this study. Detailed descriptions of the intermediate species are provided in Table S11.

| Index | Reactions | Reaction rate |
|---|---|---|

| | | |
|---|---|---|
| 11–20 | MT-aRO$_2$ + MT-aRO$_2$ → 0.893*C$_{10}$-CBYL + 0.29*C$_{10}$-ROH + 0.603*HO$_2$ + 1.34*HYDRALD + 0.067*MT-bRO$_2$ + 0.04* C$_{20}$ | 4.0e-11 |
| 21–24 | MT-aRO$_2$ + MT-bRO$_2$ → 0.96*C10-CBYL + 0.29*C10-ROH + 0.67*HO2 + 1.34*HYDRALD + 0.04* C$_{20}$ | 4.0e-11 |
| 25–28 | MT-aRO$_2$ + MT-cRO$_2$ → 0.96*C10-CBYL + 0.29*C10-ROH + 0.67*HO2 + 1.34*HYDRALD + 0.04* C$_{20}$ | 2.6e-10 |
| 29–32 | MT-aRO$_2$ + MT-HOM-RO$_2$ → 0.96*C10-CBYL + 0.29*C10-ROH + 0.67*HO2 + 1.34*HYDRALD + 0.04* C$_{20}$ | 2.6e-10 |
| 33–56 | MT-aRO$_2$ + ISOP-RO$_2$ → 0.4465*C10-CBYL + 0.145*C10-ROH + 0.145*ROH + 0.603*HO2+1.485*HYDRALD+0.0335*MT-bRO$_2$+ 0.04*C$_{15}$ | 2.0e-10 |
| 57 | MT-bRO$_2$ + MT-bRO$_2$ → 0.96*C$_{10}$-CBYL + 0.29*C$_{10}$-ROH + 0.67*HO$_2$ + 1.34*HYDRALD + 0.04* C$_{20}$ | 4.0e-11 |
| 58 | MT-cRO$_2$ + MT-cRO$_2$ → 0.96*C$_{10}$-CBYL + 0.29*C$_{10}$-ROH + 0.67*HO$_2$ + 1.34*HYDRALD + 0.04* C$_{20}$ | 2.6e-10 |
| 59 | MT-HOM-RO$_2$ + MT-HOM-RO$_2$ → 0.96*C$_{10}$-CBYL + 0.29*C$_{10}$-ROH + 0.67*HO$_2$ + 1.34*HYDRALD + 0.04* C$_{20}$ | 2.6e-10 |
| 60 | MT-bRO$_2$ + MT-cRO$_2$ → 0.96*C$_{10}$-CBYL + 0.29*C$_{10}$-ROH + 0.67*HO$_2$ + 1.34*HYDRALD + 0.04* C$_{20}$ | 2.6e-10 |
| 61 | MT-bRO$_2$ + MT-HOM-RO$_2$ → 0.96*C$_{10}$-CBYL + 0.29*C$_{10}$-ROH + 0.67*HO$_2$ + 1.34*HYDRALD + 0.04* C$_{20}$ | 2.6e-10 |
| 62 | MT-cRO$_2$ + MT-HOM-RO$_2$ → 0.96*C$_{10}$-CBYL + 0.29*C$_{10}$-ROH + 0.67*HO$_2$ + 1.34*HYDRALD + 0.04* C$_{20}$ | 2.6e-10 |
| 63–68 | MT-bRO$_2$ + ISOP-RO$_2$ → 0.48*C$_{10}$-CBYL + 0.145*C$_{10}$-ROH + 0.145*ROH + 0.67*HO$_2$ + 1.485*HYDRALD + 0.04* C$_{15}$ | 2.0e-11 |
| 69–74 | MT-cRO$_2$ + ISOP-RO$_2$ → 0.48*C$_{10}$-CBYL + 0.145*C$_{10}$-ROH + 0.145*ROH + 0.67*HO$_2$ + 1.485*HYDRALD + 0.04* C$_{15}$ | 4.0e-11 |
| 75–80 | MT-HOM-RO$_2$ + ISOP-RO$_2$ → 0.48*C$_{10}$-CBYL + 0.145*C$_{10}$-ROH + 0.145*ROH + 0.67*HO$_2$ + 1.485*HYDRALD + 0.04* C$_{15}$ | 4.0e-11 |

### 2.2.4 $C_{10}$ HOMs formation

When MT-HOM-$RO_2$ are oxidized by $HO_2$, NO, or $NO_3$ (Fig. 3), three types of gas-phase $C_{10}$ HOMs are formed: two types of $C_{10}$ non-nitrate HOMs ($C_{10}$-aNON and $C_{10}$-bNON) and $C_{10}$ nitrate HOMs ($C_{10}$-ON ), as shown in Table 6. The rate constants used are the same as those for the MT-$RO_2$ + $HO_2$, NO, and $NO_3$ reactions in Xu et al. (2022).

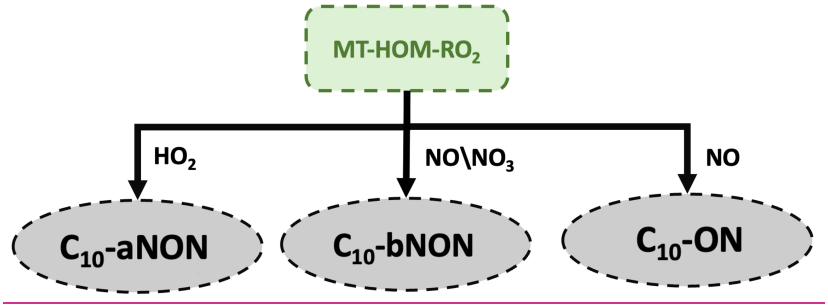


**Figure 3**. Schematic diagram illustrating the oxidation of MT-HOM-$RO_2$ by $HO_2$, NO, or $NO_3$, leading to the formation of three types of gas-phase $C_{10}$-HOMs.

**Table 6.** $C_{10}$ HOMs formation. Detailed descriptions of the intermediate species are provided in Table S11.

| Index | Reactions | Reaction rate |
|---|---|---|
| 109 | MT-HOM-$RO_2$ + $HO_2$ → $C_{10}$-aNON + $O_2$ | 1.5e-11 |
| 110 | MT-HOM-$RO_2$ + NO → 0.8*$NO_2$ + 0.8*$HO_2$ + 0.4* $C_{10}$-bNON + 0.8*HYDRALD + 0.2* $C_{10}$-ON | 4.0e-12 |
| 111 | MT-HOM-$RO_2$ + $NO_3$ → $HO_2$ + $NO_2$ + 0.5* $C_{10}$-bNON + HYDRALD | 1.2e-12 |

### ~~2.4~~2.3 Observations

~~This study utilizes observational data from the Southeast Nexus (SENEX) (Warneke et al., 2016) and Biogenic Aerosols-Effects on Clouds and Climate (BAECC) (Petäjä et al., 2016) field campaigns (Table 3). The observed variables include NO, $O_3$, monoterpenes, isoprene (ISOP), HOMs with 10 carbon atoms ($C_{10}$), and particle-phase $C_{10}$ concentrations. Further details regarding the field campaigns can be found in Text S2 of Xu et al. (2022).~~ Data from two campaigns were used for comparison: the Southern Oxidant and Aerosol Study (SOAS) in the southeastern USA, and the Biogenic Aerosols – Effects on Clouds and Climate (BAECC) in Hyytiälä, Finland (Carlton et al., 2018; Petäjä et al., 2016) (Table 7). HOM measurements were obtained using high-resolution time-of-flight chemical ionization mass spectrometer (HRToF-CIMS) when available {Lopez-Hilfiker,

2014 #707}(Lopez-Hilfiker et al., 2014). For HOM measurements, molecular formulas of compounds containing 10 carbon atoms and at least 7 oxygen atoms were selected as HOMs. The compounds with one nitrate and without nitrate were compared to the simulated $C_{10}$-aNON, $C_{10}$-bNON, and $C_{10}$-ON, respectively. In addition to HOMs, related species such as NO, $O_3$, monoterpenes, and isoprene were also compared when the data was available (Figs. S1 and S2). The primary HOM species identified in the SENEX (Southeast Nexus) and BAECC campaigns (Tables S15 and S16).

~~**Table 3**~~**Table 7.** Field campaigns used in this paper

| Campaigns | Dates | Locations |
|---|---|---|
| ~~SENEX~~ SOAS (Warneke et al., 2016) | 2013.06.01–07.15 | Centreville, Alabama, US (32.93°N, 87.13°W) |
| BAECC (Petäjä et al., 2016) | 2014.04.11–06.03 | Station for Measuring Ecosystem Atmosphere Relations (SMEAR II), Hyytiälä, Finland. (61.85°N，24.28°E) |

### ~~2.3~~ 2.4 Sensitivity experiments

The formation of monoterpene-derived HOMs involves two key uncertainties: (1) the branching ratios of autoxidation-capable peroxy radicals (MT-b$RO_2$) formed via OH- and $O_3$-initiated oxidation (Lee et al., 2023; Weber et al., 2020; Pye et al., 2019; Xu et al., 2019; Piletic and Kleindienst, 2022), and (2) the autoxidation rate of MT-b$RO_2$, which varies by over an order of magnitude in experimental studies (Berndt et al., 2018; Roldin et al., 2019; Weber et al., 2021). To systematically analyze these uncertainties, we conducted nine sensitivity experiments (~~Table 2~~ Table 8). The Control experiment adopts the branching ratios from Xu et al. (2022) (MT-b$RO_2$: 75% for OH-initiated and 8% for $O_3$-initiated reactions), serving as a benchmark aligned with recent mechanistic frameworks. Four additional experiments (LowYield, HighYield, HighOH_Low$O_3$, LowOH_High$O_3$) span the full parameter space of MT-b$RO_2$ branching ratios reported in literature (OH: 7.5–83%; $O_3$: 0.01–22%) (Saunders et al., 2003; Roldin et al., 2019; Rolletter et al., 2019), while two experiments (Fast and Slow) explore autoxidation rate extremes (×10 and ×0.1 of the Control rate). To isolate pathway-specific uncertainties in the formation of nitrate HOMs containing 10 carbons ($C_{10}$-ON) (Bianchi et al., 2019; Yan et al., 2016; Xu et al., 2022; Weber et al., 2020), we further test NO-mediated HOM formation (no_HMB_NO) (Reaction 110 in Table ~~S7~~6). Besides, in comparison with the SENEX and BAECC field campaigns, the simulated NO concentration in the Control experiment is overestimated by a factor of four (Figs. S1 and S2). Therefore, we multiplied the ~~NOx~~NO emissions by 0.2 in the ~~LowNOx~~ LowNO experiment to assess the impact of anthropogenic ~~NOx~~NO on HOM concentration. ~~These experiments collectively quantify how mechanistic uncertainties propagate to HOMs predictions, bridging gaps between chamber-derived parameters and global model~~

~~applications.~~ These experiments help quantify how uncertainties in chemical mechanisms affect HOM concentrations in global models.

**Table ~~2~~8.** Experiments used in this paper.

| Experiments | OH branching ratio | $O_3$ branching ratio | Autoxidation rate | RO pathway | ~~NOx~~NO emissions |
|---|---|---|---|---|---|
| Control | 75% | 8% | $K_{auto}$[a] | √ | default |
| LowYield | 7.5% | 0.01% | | | |
| HighYield | 83% | 22% | | | |
| HighOH_lowO3 | 83% | 0.01% | | /[b] | |
| LowOH_HighO3 | 7.5% | 22% | | | |
| Fast | / | | $10\times K_{auto}$ | / | |
| Slow | | | $0.1\times K_{auto}$ | | |
| no_HMB_NO | / | | | X[c] | / |
| ~~LowNOx~~ LowNO | / | | | | default/5 |

[a] The specific values of $K_{auto}$ are provided in Table 4
[b] The setting is the same as Control
[c] The yield of ~~b~~$C_{10}$-bNON is set to zero in the MT-HOM-$RO_2$ + NO reaction (reaction 110 in Table ~~S7~~6)

## 3 Results

### 3.1 Model evaluation

The revised model successfully captures the observed diurnal patterns of total HOMs ($C_{10}$-ON + $C_{10}$-NON), despite systematic biases in the concentrations of individual components. Most sensitivity tests underestimate nitrate HOMs ($C_{10}$-ON) by 20–50% and overestimate non-nitrate HOMs ($C_{10}$-NON) by approximately 30% (~~Table 2~~ Figs. 4 and 5), but they effectively reproduce the observed diurnal cycles (Figs. 4 and 5). Observations indicate that $C_{10}$-ON concentrations peak around midday, while $C_{10}$-NON shows minimal variation throughout the day. The simulations align well with these patterns: all experiments capture the morning rise in total $C_{10}$-ON (Figs. 4b and 5b), driven by NO accumulation and increased photochemical activity (Figs. S1 and S2). The diurnal evolution of the boundary layer height (BLH) also plays a significant role in modulating HOMs concentrations. The morning expansion of the BLH enhances vertical mixing, diluting HOMs near the surface, while its afternoon collapse concentrates HOMs in a shallower layer, amplifying their observed peaks. Meanwhile, $C_{10}$-NON trends

remain relatively flat (within ±15% of daily means), as their formation is influenced by the competing effects of OH (morning peak), $O_3$ (afternoon peak), and monoterpene emissions (which vary throughout the day) (Figs. S1 and S2).

Simulations with increased MT-bRO$_2$ branching ratios and autoxidation rates (HighOH_LowO$_3$, HighYield, Fast) captured $C_{10}$-ON peak concentrations more accurately, whereas simulations with reduced branching ratios and autoxidation rates (LowYield, LowOH_HighO$_3$, Slow) showed better agreement with observed $C_{10}$-NON levels at both sites. Specifically, the HighOH_LowO$_3$, HighYield, Fast, and Control experiments overestimated total $C_{10}$ by ~50% (Figs. 4a and 5a) but reproduced $C_{10}$-ON peaks within observational uncertainty (Figs. 4b and 5b). Conversely, the LowYield, LowOH_HighO$_3$, and Slow experiments underestimated total $C_{10}$ but aligned more closely with $C_{10}$-NON concentrations (Figs. 4c and 5c). These results underscore the necessity of tailoring MT-bRO$_2$ branching ratios to specific oxidation pathways ($C_{10}$-ON and $C_{10}$-NON) for accurate $C_{10}$ modeling. However, current uncertainties in autoxidation kinetics and the scarcity of pathway-resolved observational data (e.g., real-time measurements of RO$_2$ intermediates) limit our ability to further constrain these parameters (Berndt et al., 2018; Weber et al., 2021; Xu et al., 2022). ~~Addressing these gaps requires coordinated laboratory measurements and targeted ambient observations to disentangle competing chemical processes.~~

Compared to the dominant uncertainties in MT-bRO$_2$ branching ratios, the impacts of NO~~NOx~~ emissions and NO-mediated $C_{10}$-NON formation pathways are less significant, though they provide complementary insights into HOM chemistry. In the ~~LowNOx~~LowNO sensitivity experiment, total $C_{10}$ concentrations decreased from 736 to 339 ng/m$^3$ at the Centreville site (anthropogenically influenced) due to reduced ~~NOx~~NO emissions, with $C_{10}$-ON showing a more pronounced reduction (117 to 30 ng/m$^3$) than $C_{10}$-NON (619 to 310 ng/m$^3$), consistent with the NO-dependent formation of $C_{10}$-ON (~~Figs. 2 and 3~~ Fig. 3 and Table 6). In contrast, at the SMEAR II site, total $C_{10}$ remained nearly unchanged (141 to 142 ng/m$^3$), reflecting minimal NO~~NOx~~ influence in the pristine region. Similarly, the no_HMB_NO experiment, which eliminates NO-mediated $C_{10}$-NON production, reduced $C_{10}$-NON concentrations by about 40% (619 to 398 ng/m$^3$ at Centreville; 112 to 57 ng/m$^3$ at SMEAR II) and improved agreement with observations (Figs. 4c and 5c).

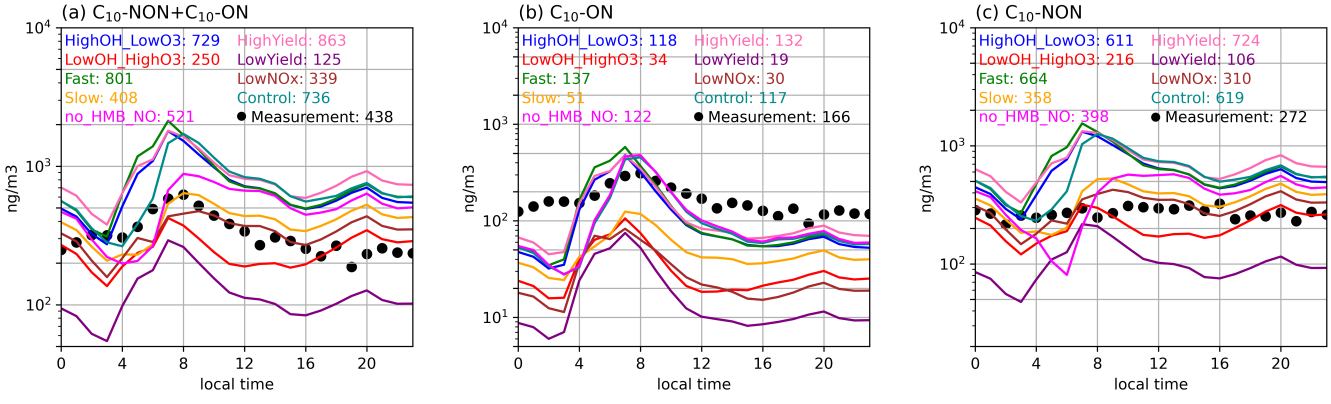

~~**Figure 1.** Figure 4. The diurnal cycle of observed (dots) surface and simulations (solid lines) total $C_{10}$ ($C_{10}$-ON+ $C_{10}$-NON) (a), $C_{10}$-ON (b) and $C_{10}$-NON (c) concentrations (unit: ng/m$^3$) at the Centreville site during the SENEX campaign. The simulated surface $C_{10}$ ($C_{10}$-ON and $C_{10}$-NON) concentrations at the closest grid to the Centreville site are used from simulations (solid lines). The simulated $C_{10}$ at two sites are scaled by the ratios of the observed monoterpene concentrations to the simulated monoterpene concentrations ($R_{MT}$, Figure S1a and S2a). The Normalized Mean Bias (NMB), Correlation Coefficient (R), and Root Mean Square Error (RMSE) values of $C_{10}$ comparing with observation are shown in Table S13. The $C_{10}$, $C_{10}$-NON and $C_{10}$-ON concentrations are the sum of gas phase and particle phase concentrations.~~ Diurnal variations of observed (dots) and simulated (solid lines) surface concentrations of (a) total $C_{10}$ ($C_{10}$-aON + $C_{10}$-bON + $C_{10}$-NON), (b) $C_{10}$-aON + $C_{10}$-bON, and (c) $C_{10}$-NON at the Centreville site. Simulations are scaled by the observed-to-simulated monoterpene ratios (see Figures S1a and S2a). All concentrations (ng/m³) include both gas and particle phases. Numbers shown represent daily mean values. Sensitivity experiment information is provided in Table 8. Model performance metrics (NMB, R, RMSE) are provided in Table S12.

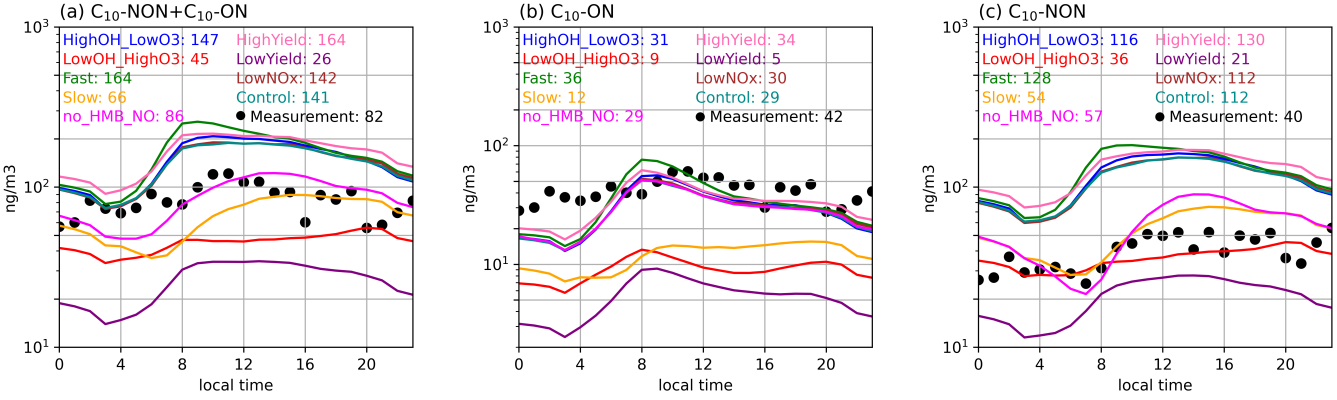


~~**Figure 3.** Figure 5. The diurnal cycle of observed (dots) surface $C_{10}$ ($C_{10}$-ON+ $C_{10}$-NON) (a), $C_{10}$-ON (b) and $C_{10}$-NON (c) concentrations (unit: ng/m$^3$) the SMEAR II sites during the BAECC campaign. The simulated surface $C_{10}$ ($C_{10}$-ON and $C_{10}$-NON) concentrations at the closest grid to the SMEAR II site are used from different simulations (solid lines). The simulated $C_{10}$ at two sites are scaled by the ratios of the observed monoterpene concentrations to the simulated monoterpene concentrations ($R_{MT}$, Figure S1a and S2a). The Normalized Mean Bias (NMB), Correlation Coefficient (R), and Root Mean Square Error (RMSE) values of $C_{10}$ comparing with observation are shown in Table S13. The $C_{10}$, $C_{10}$-NON and $C_{10}$-ON concentrations are the sum of gas phase and particle phase concentrations.~~ Diurnal variations of observed (dots) and simulated (solid lines) surface concentrations of (a) total $C_{10}$ ($C_{10}$-aON + $C_{10}$-bON + $C_{10}$-NON), (b) $C_{10}$-aON + $C_{10}$-bON, and (c) $C_{10}$-NON at the SMEAR II site. Simulations are scaled by the observed-to-simulated monoterpene ratios (see Figures S1a and S2a). All concentrations (ng/m³) include both gas and particle phases. Numbers shown represent daily mean values. Sensitivity experiment information is provided in Table 8. Model performance metrics (NMB, R, RMSE) are provided in Table S12.

### 3.2 Main formation pathways of HOMs

Previous modeling studies on HOMs (Xu et al., 2022; Weber et al., 2021) have focused on isolated pathways or fixed parameters, limiting their capacity to resolve competing chemical mechanisms under varying environmental conditions. Our study advances this approach by conducting nine targeted sensitivity experiments that collectively investigate how MT-bRO$_2$ branching ratios, autoxidation rates, and NO~~NOx~~ perturbations differentially influence the steering of HOMs toward distinct formation pathways (~~Table 2~~ Fig. 3).

$C_{10}$-ON and $C_{10}$-NON formation pathways exhibit distinct dependencies on oxidant availability and autoxidation kinetics. $C_{10}$-ON is exclusively formed via NO termination of MT-HOM-RO$_2$ radicals, whereas $C_{10}$-NON arises predominantly from MT-

HOM-$RO_2$ reactions with $HO_2$ (~64%) and NO (~35%) (~~Fig. 4~~Fig. 6). This $HO_2$-dominated pathway to form $C_{10}$-NON remains robust across sensitivity tests (61~72% contribution), with the Slow experiment showing the highest $HO_2$ contribution. These results align with Xu et al. (2022), who identified $HO_2$ as a key driver of non-nitrate HOMs, but extend their findings by quantifying NO's role in terminating $C_{10}$ pathways.

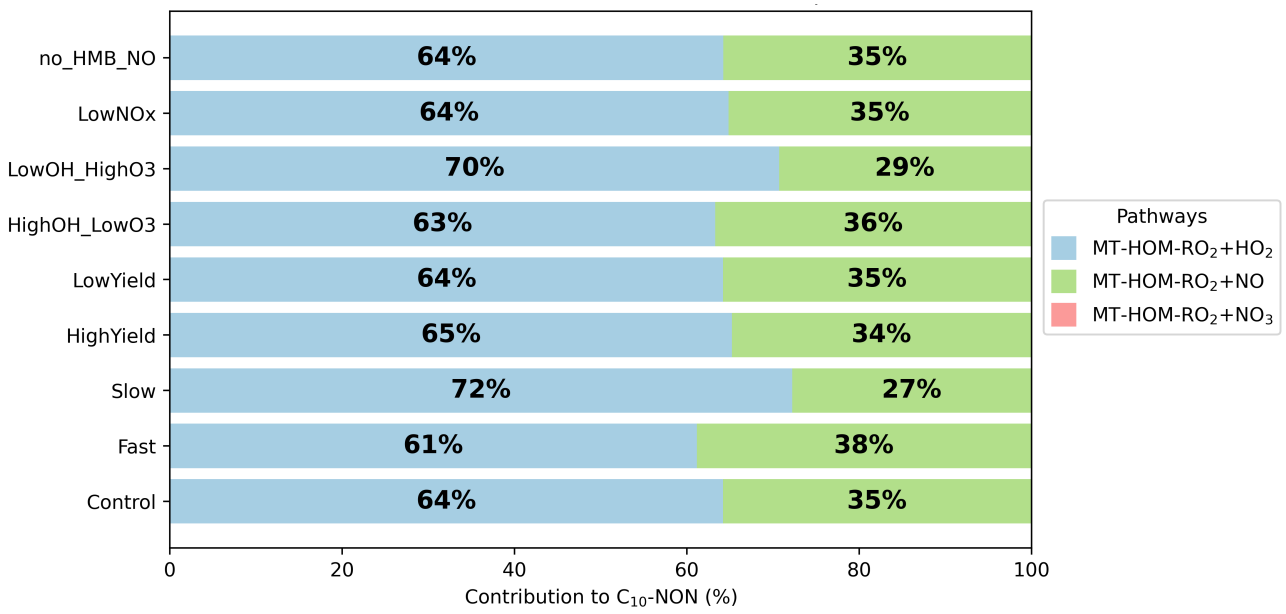


**~~Figure 4~~ Figure 6.** Contribution of different reaction pathways using different sensitivity tests (~~Table 2~~Table 8) to form $C_{10}$-NON (non-nitrate HOMs containing 10 carbons). "MT-HOM-$RO_2$+$HO_2$", "MT-HOM-$RO_2$+NO" and "MT-HOM-$RO_2$+$NO_3$" refer to Reactions 109, 110 and 111 in Table 6.

The formation of $C_{15}$ and $C_{20}$ is governed by cross-reactions involving MT-$RO_2$ and isoprene-derived radicals (ISOP-$RO_2$), with sensitivity to MT-b$RO_2$ branching ratios and autoxidation rates. In the Control experiment, cross-reactions between MT-a$RO_2$/MT-HOM-$RO_2$ and ISOP-$RO_2$ account for 97% of $C_{15}$ (~~Fig. 5~~Fig. 7). When MT-b$RO_2$ branching ratios are enhanced (HighYield), MT-HOM-$RO_2$ concentrations increase, shifting $C_{15}$ formation from MT-a$RO_2$–ISOP-$RO_2$ (ranging from 35% to 47%) to MT-HOM-$RO_2$–ISOP-$RO_2$ (ranging from 50% to 62%), while $C_{20}$ formation shifts from MT-a$RO_2$ self-reactions (ranging from 11% to 21%) to MT-HOM-$RO_2$ self-reactions (ranging from 27% to 38%).

~~Autoxidation rates critically regulate the formation pathways of accretion product generation by directly affecting the concentration of MT-HOM-$RO_2$.~~ Autoxidation rates also influence the formation pathways of accretion products by affecting the distribution of peroxy radical intermediates. In the Slow experiment (×0.1 autoxidation rate), reduced MT-HOM-$RO_2$ production decreases its self-reaction contribution to $C_{20}$ formation by 44% (from 27% to 15%) and cross-reactions contribution to $C_{15}$ by 26% (from 50% to 37%). Conversely, the Fast experiment (with a 10-fold increase in the autoxidation rate) amplifies these contributions by 7% ($C_{20}$) and 4% ($C_{15}$), demonstrating a nonlinear response to rate changes. This differs

from the approach of Weber et al. (2021), who assumed fixed branching ratios ~~for~~ to form accretion products and did not account for the dynamic interplay between autoxidation and cross-reaction kinetics highlighted in this study.

Anthropogenic NO~~NOx~~ emissions and NO-mediated $C_{10}$-NON pathways have minimal influence on $C_{15}/C_{20}$ formation (<1% variability), underscoring the dominance of MT-b$RO_2$ branching uncertainties. The ~~LowNOx~~ LowNO and no_HMB_NO experiments show negligible changes in accretion pathways, as NO~~NOx~~ perturbations primarily alter terminal products ($C_{10}$-ON/$C_{10}$-NON) rather than radical pools. This contrasts with Xu et al. (2022), who emphasized NO~~NOx~~-driven HOM variability but did not isolate its limited impact on accretion chemistry.

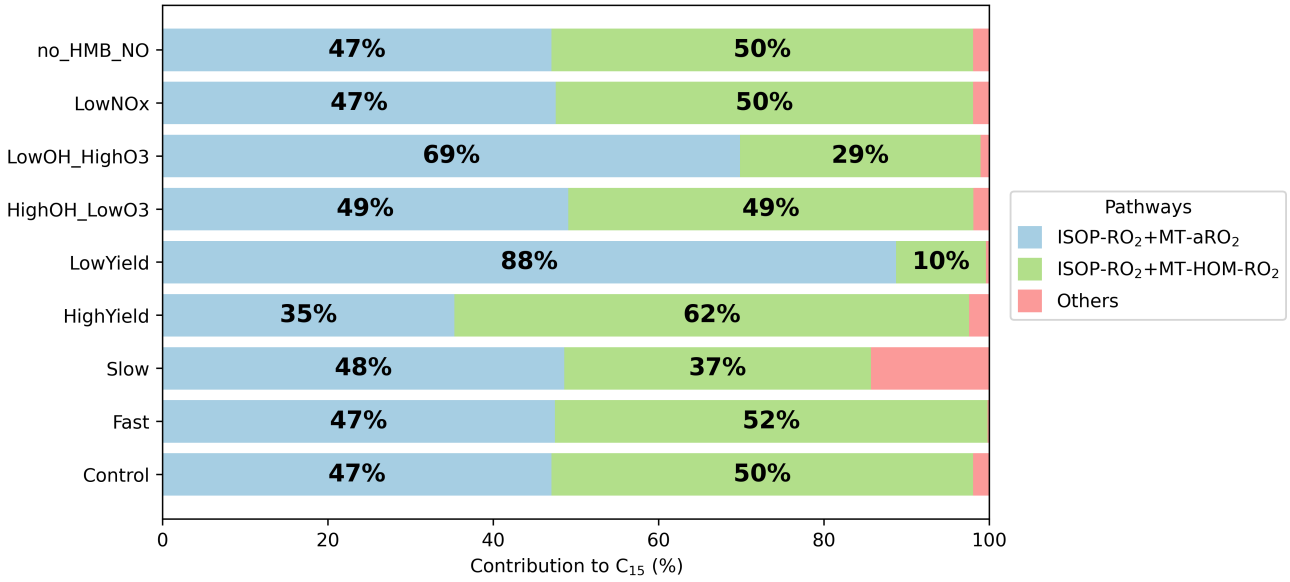


**Figure ~~5~~7.** Contribution of different reaction pathways using different sensitivity tests (Table 8) to form $C_{15}$ (HOMs containing 15 carbons). "ISOP-$RO_2$+MT-a$RO_2$" and "ISOP-$RO_2$+MT-HOM-$RO_2$" refer to Reactions 33-56 and 75-80 in Table 5. "others" refers to other reactions forming $C_{15}$ in Table 5.

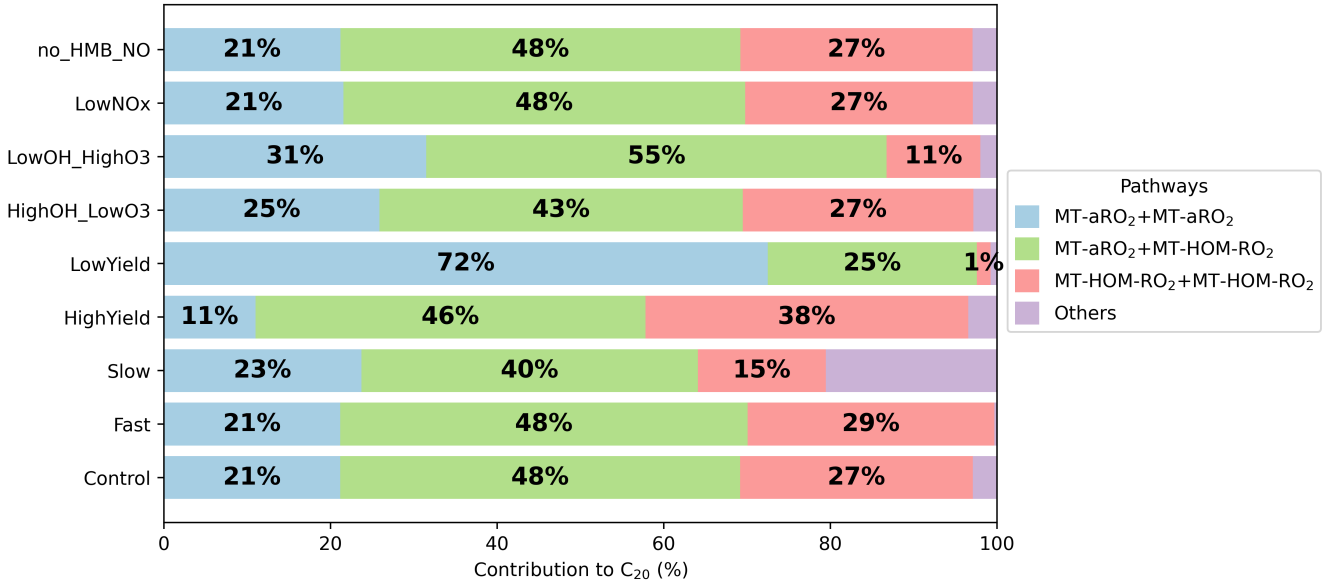


**Figure ~~6~~8.** Contribution of different reaction pathways using different sensitivity tests (Table 8) to form $C_{20}$ (HOMs containing 20 carbons). "MT-a$RO_2$+MT-a$RO_2$", "MT-a$RO_2$+MT-HOM-$RO_2$" and "MT-HOM-$RO_2$+MT-HOM-$RO_2$" refer to Reactions 11-20, 29-32 and 59 in Table 5. "others" refers to other reactions forming $C_{20}$ in Table 5.

## 4 Spatial and temporal distribution of HOMs-SOA

### 4.1 Spatial and distribution of HOMs-SOA

Globally, the annual mean concentration of HOMs-SOA is 0.0556 μg $m^{-3}$, accounting for 13.3 % of total SOA and 37.3 % of MTSOA (Fig. 12). Across the sensitivity experiments, the contribution of HOMs-SOA to total SOA varies between 6 % and 15 % (Fig. 9). The HighYield (15 %) and LowYield (6 %) experiments encompass the uncertainty range reported in Xu et al. (2022) and highlight the dominant influence of the MT-b$RO_2$ branching ratio on HOMs-SOA formation. The effect of autoxidation rates is secondary, as indicated by the Fast (14 %) and Slow (10 %) experiments (Fig. 12), where the differences are moderate and consistent with the rate-dependent parameterizations proposed by Weber et al. (2021). In contrast, the influence of NO levels is negligible, with the LowNO (13 %) and no_HMB_NO (11 %) experiments indicating that anthropogenic NO emissions exert little impact on the global HOMs-SOA concentration. Similarly, the contribution of HOMs-SOA to MTSOA ranges from 19 % to 41 % across the sensitivity experiments, with the highest fraction in HighYield and the lowest in LowYield, further highlighting the critical role of the MT-b$RO_2$ branching ratio in determining the HOMs-SOA contribution.

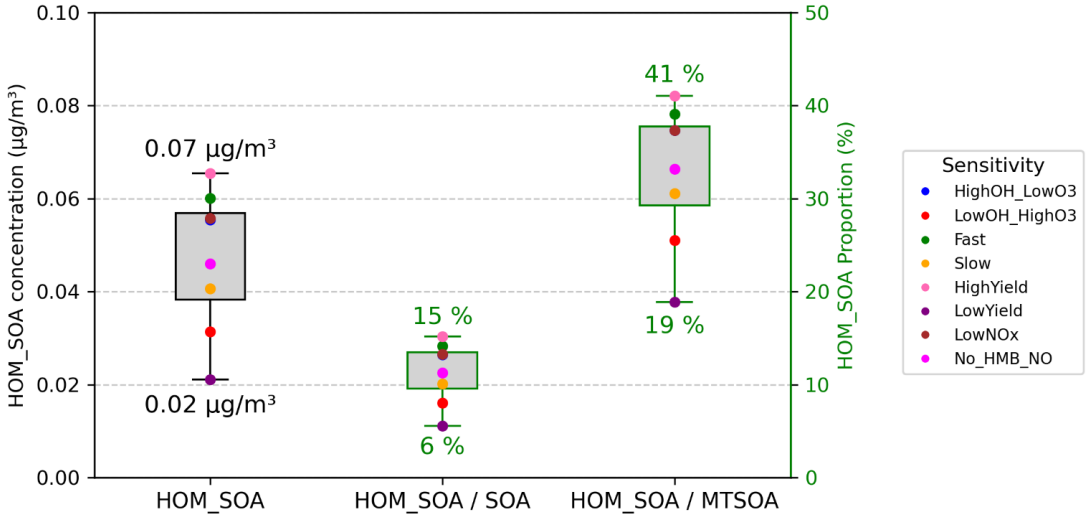


**Figure 9.** The global averaged value of 2013 annual mean surface HOMs-SOA (unit: µg/m3), the contribution of HOMs-SOA to the total SOA and MTSOA (unit: %) using different sensitivity tests (Table 8). The specific value of different tests is shown in Table S13.

The contribution of HOMs-SOA to total SOA and MTSOA shows pronounced spatial variability globally (Fig. 10). In the Control experiment, HOMs-SOA concentrations are highest in tropical and parts of mid-latitude regions, particularly over the Amazon rainforest, central Africa, the southeastern United States, and Australia, where warm and humid conditions coincide with high biogenic emissions (Fig. 10a). In these regions, HOMs-SOA typically accounts for more than 10 % of total SOA, with some areas exceeding 40 % (Fig. 10b), and contributes more than 20 % to MTSOA (Fig. 10c). Also, in regions strongly influenced by anthropogenic emissions, such as Southeast Asia and Europe, the contribution of HOMs-SOA to MTSOA remains substantial, consistent with the role of anthropogenic NO in HOM formation (Fig. 3).

Across the sensitivity experiments, the spatial patterns of HOMs-SOA contributions to total SOA and MTSOA are generally consistent with those in the Control experiment (Fig. S5). In the HighYield experiment, the contribution of HOMs-SOA to MTSOA exceeds 30 % over most tropical regions with high biogenic emissions. In contrast, in the LowYield experiment, the contribution to MTSOA drops markedly across most regions, falling below 15 %. These results indicate that uncertainties in the MT-bRO$_2$ branching ratio not only affect the global mean but also amplify the contrast between biogenically dominated regions and other areas. Changes in the Fast and Slow experiments are more moderate, occurring mainly over high-emission regions and their downwind areas, where Fast increases the HOMs-SOA contribution to MTSOA by ~5%, while Slow yields comparable decreases. By comparison, the NO-related experiments (LowNO and no_HMB_NO) show limited changes in most regions, with slight decreases (< 2%) in both MTSOA and total SOA contributions over high-NO emission regions such as East Asia and Europe. These results further support that, although NO can alter HOM composition under polluted conditions, its influence on the global burden and spatial distribution of HOMs-SOA is minimal.

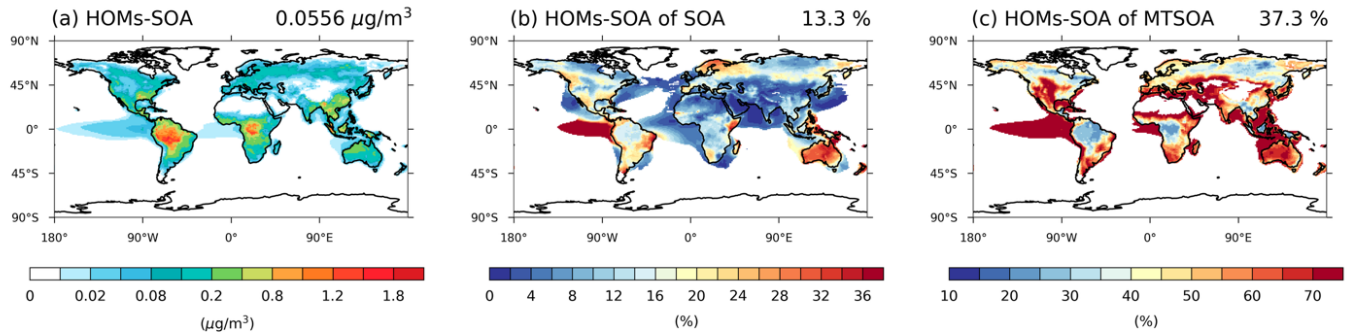


**Figure 10.** 2013 annual averaged surface (a) HOMs-SOA (unit: μg/m3), (b) the contribution of HOMs-SOA to the MTSOA and (c) the contribution of HOMs-SOA to the total SOA (unit: %) in Control experiment. The global averaged value is shown in upper right corner of each figure. Proportions are only shown in regions where MTSOA or total SOA is greater than 10% of the global average.

Vertically, HOMs-SOA is primarily concentrated in the near-surface and lower troposphere (below 800 hPa), reflecting its close link to surface biogenic emissions (Fig. 11). There are significant regional differences in the contribution of HOMs-SOA to total SOA between the Northern and Southern Hemispheres. In most regions of the Northern Hemisphere, anthropogenic emissions dominate, leading to a low contribution from biogenic HOMs-SOA (<10%). In contrast, the contribution increases markedly in the Southern Hemisphere (>14%). This difference is largely driven by the high emissions of monoterpenes and isoprene in tropical regions, such as the Amazon and central Africa (Fig. S3), which promote the substantial formation of HOMs-SOA, especially $C_{15}$ and $C_{20}$ (Fig. 12). These compounds are then transported to higher altitudes through deep convection. As a result, HOMs-SOA remains at high concentrations in the 400–200 hPa range in the tropics, contributing more than 20% to SOA at these altitudes (Fig. 11). Additionally, gaseous HOMs may also be transported to higher layers, where they significantly enhance new particle formation, influencing cloud condensation nuclei (CCN) concentrations (Shao et al., 2024; Zhao et al., 2024), and further affecting cloud properties and radiative effects (Shao et al., 2025).

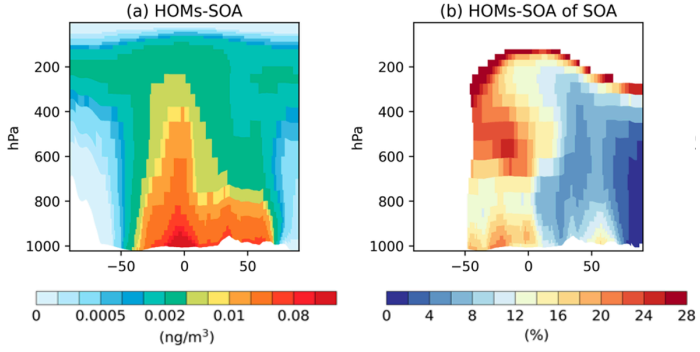


**Figure 11.** Vertical distribution of 2013 annual averaged (a) HOMs-SOA concentration (μg/m³) and (b) proportion of HOMs-SOA to total SOA (%) in the Control experiment. The global average value is shown in the upper right corner of each panel. Proportions are only shown in regions where total SOA is greater than 10% of the global average.

### 4.2 Temporal variation of HOMs-SOA

On a global scale, the seasonal variation of HOMs-SOA are primarily determined by the intensity of biogenic emissions (monoterpenes and isoprene), with a more significant effect in the Northern Hemisphere summer (Fig. 13). The levels of oxidants (OH and $O_3$), however, play a greater role in modulating the relative contribution of different HOM species (Figs. 12 and 14). In high NO regions, such as the United States (US), Southeast Asian continental regions (SECN), and Europe (EUR), the concentrations of OH and $O_3$ facilitate the formation of MT-HOM-$RO_2$. Combined with higher NO concentrations, this promotes the generation of $C_{10}$-ON (Fig. 3). In contrast, in low NO tropical regions, such as the Amazon and central Africa (CAF), the proportion of low-volatility dimers ($C_{15}$ and $C_{20}$) significantly increases.

In tropical regions, the absolute concentration of HOMs-SOA is significantly higher than in mid-latitudes, with a greater proportion of dimers ($C_{15}$ and $C_{20}$) (Fig. 12). The annual mean concentration in the AMZ is 0.90 μg/m³, peaking during the dry season (August–October) at approximately 1.4 μg/m³. During this period, monoterpene (~230 ng/m³) and isoprene (~900 ng/m³) emissions are elevated (Fig. 13), while reduced wet deposition favors the formation of $C_{15}$ and $C_{20}$ dimers. As a result, the dimer fraction reaches 58%, with $C_{15}$ contributing 34% and $C_{20}$ contributing 24%. $O_3$ concentrations (Fig. 14) also promote multi-step autoxidation reactions. Meanwhile, the relatively low anthropogenic emissions in the Amazon result in low NO concentrations, preventing the rapid formation of $C_{10}$-ON via NO reactions with MT-HOM-$RO_2$ (Fig. 3). Instead, MT-HOM-$RO_2$ undergoes self- and cross-reactions to form dimers. Similarly, the CAF region exhibits similar characteristics, with an annual mean concentration of 0.47 μg/m³, maintaining relatively high levels throughout the year. During the peak emission period (January–May), both $C_{15}$ and $C_{20}$ levels increase simultaneously (Fig. 12). These findings highlight that low NO emissions and high biogenic emissions play an important role in the generation dimers.

Mid-latitude regions exhibit significant seasonal variations, with a higher proportion of $C_{10}$-ON (Fig. 12). In regions such as the US, SECN, and EUR, a clear summer peak occurs between June and August, corresponding to significant increases in monoterpene and isoprene emissions (Fig. 13). South Asia (SAS) shows a bimodal distribution, with higher emissions in March–May and October–November, respectively. During the rainy season (June–September), enhanced wet deposition leads to reduced biogenic emissions, resulting in a bimodal distribution of HOMs-SOA (Fig. 13). In the Southern Hemisphere, Australia (AUS) exhibits a seasonal peak opposite to that of the Northern Hemisphere (occurring from October to March) (Fig. 13), but the seasonal distribution still remains consistent with biogenic emissions (Fig. 13). In these regions, where anthropogenic NO emissions are high, the proportion of $C_{10}$-ON (exceeding 60%) is significantly higher than that of dimers, highlighting the dominant role of the MT-HOM-$RO_2$ + NO termination reaction under high NO conditions.

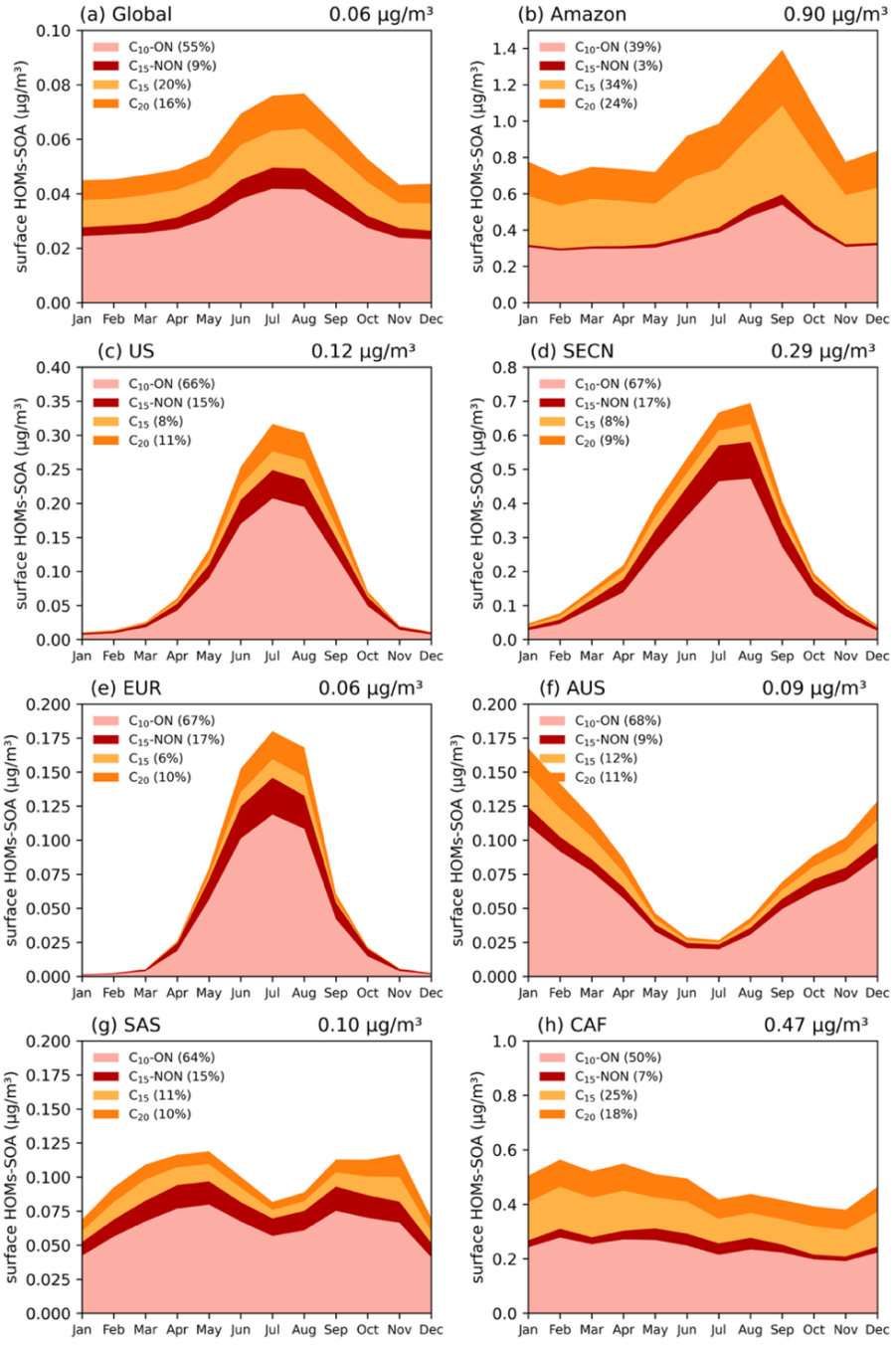


460

**Figure 12.** Seasonal variations of HOMs-SOA concentrations (μg/m³) in different regions. The contributions of $C_{10}$-ON, $C_{10}$-NON, $C_{15}$, and $C_{20}$ are shown in different colors, with the percentage contribution of each component indicated in the legend. Details of each geographic region can be found in Figure S6.

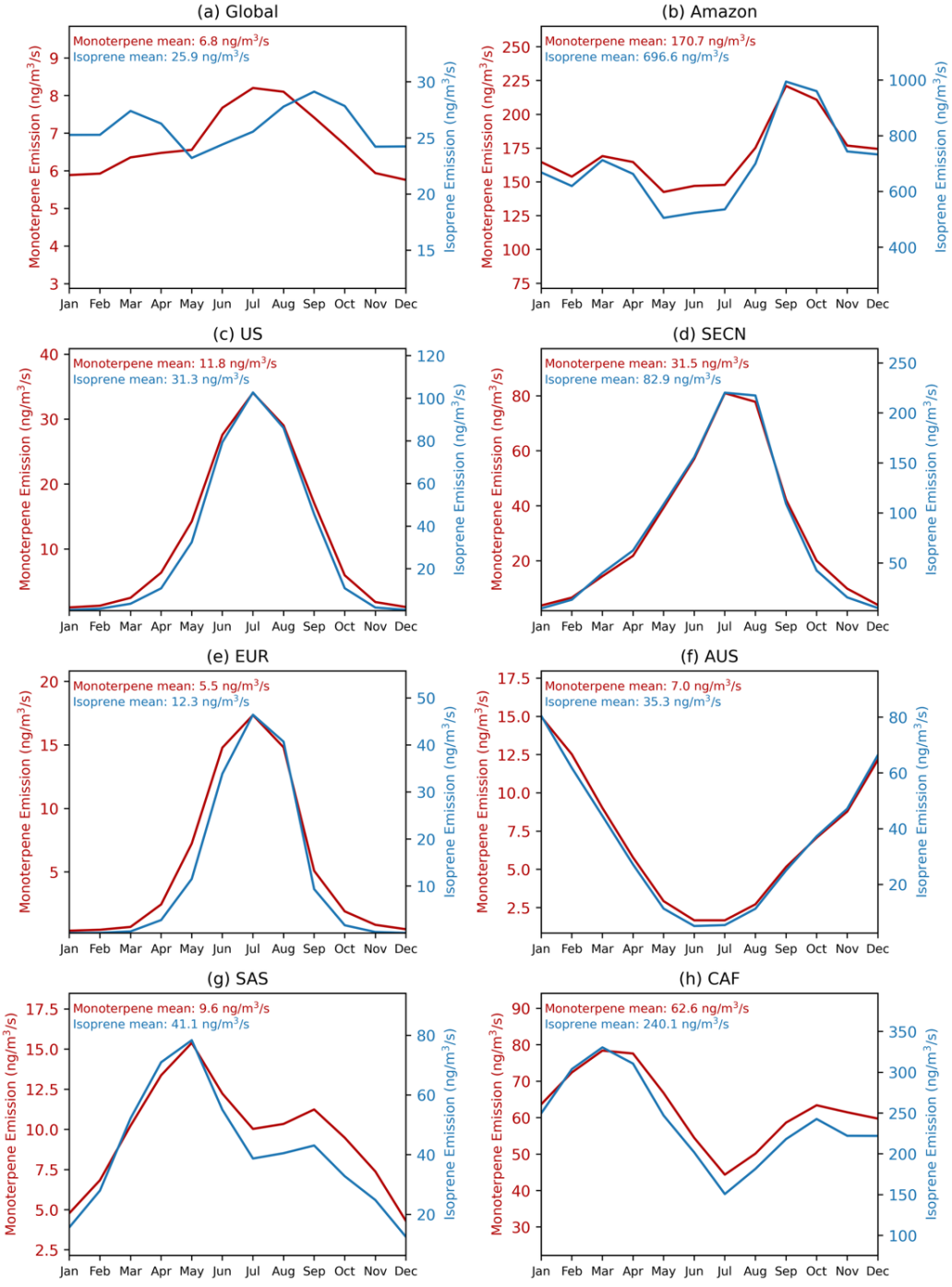


**Figure 13.** Seasonal variations in monoterpene and isoprene emissions (ng/m³/s) across different regions. The average annual emissions for each species are provided in the caption. Details of each geographic region can be found in Figure S6.

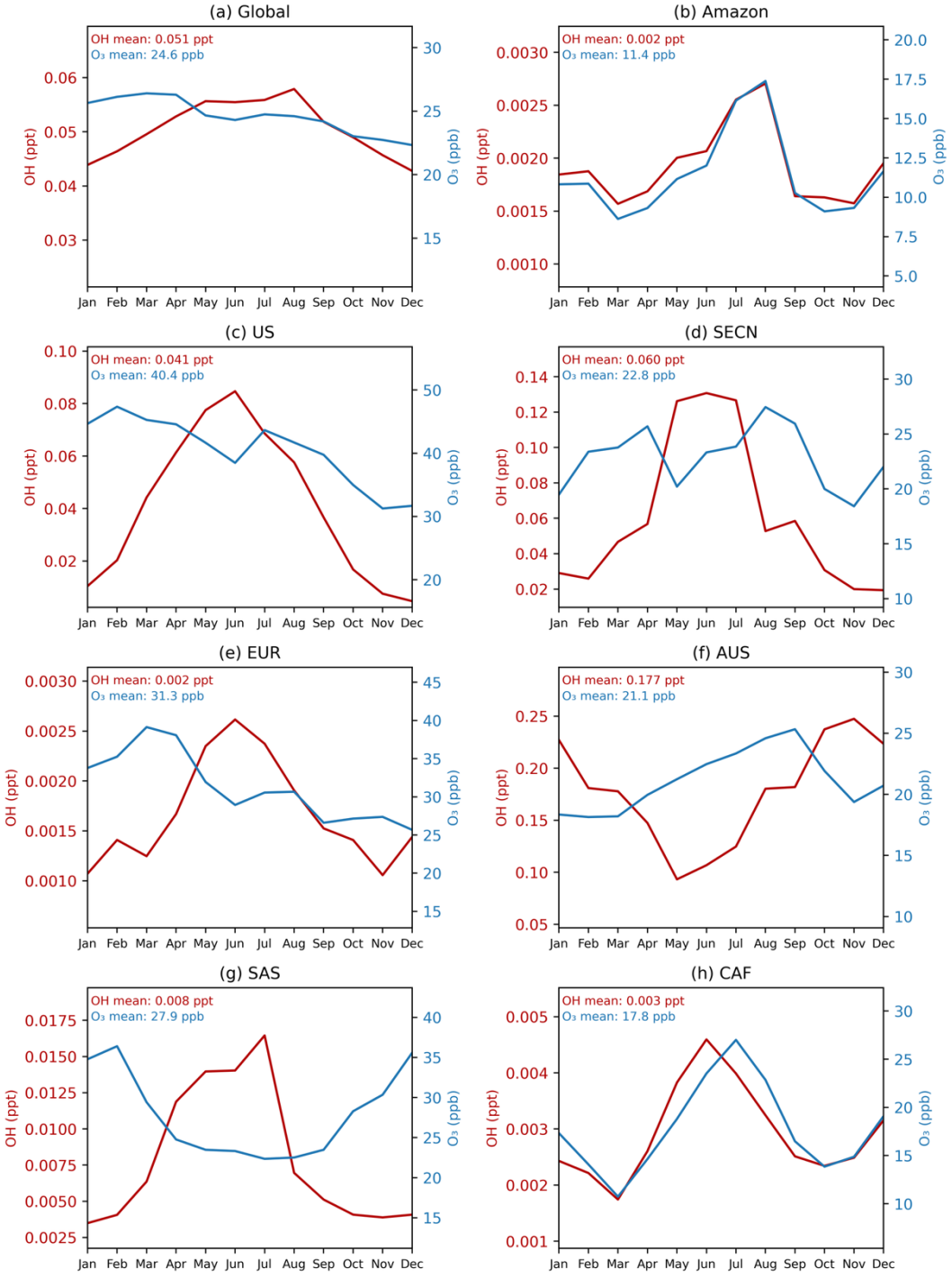


**Figure 14.** Seasonal variations of OH and $O_3$ concentrations (ppt and ppb) in different regions. The mean OH and $O_3$ values for each region are shown in the upper right corner of each panel. Details of each geographic region can be found in Figure S6.

## 5 Conclusions

The advanced chemical mechanism is coupled with CAM6-Chem model to provide a comprehensive understanding of the formation and spatiotemporal distribution of Highly Oxygenated Organic Molecules (HOMs). Unlike fixed-yield or fixed-branch approaches (Gordon et al., 2016; Gordon et al., 2017; Zhu et al., 2020; Weber et al., 2021; Zhao et al., 2024), our updated model with semi-explicit HOMs chemistry and sensitivity experiments captures pathway-specific dependencies, revealing nonlinear responses to the branching ratio of MT-b$RO_2$ (monoterpene-derived peroxy radicals which can undergo autoxidation), anthropogenic NO~~NOx~~ emission and autoxidation kinetics. By resolving $C_{10}$ (HOMs containing 10 carbons), $C_{15}$ (HOMs containing 15 carbons), and $C_{20}$ (HOMs containing 20 carbons) component, we advance beyond lumped HOMs classifications (e.g. "ELVOC" in Zhu et al. (2019) and Zhao et al. (2024)), enabling a more targeted analysis of contributions from various biogenic sources.

The improved model generally captures the observed diurnal cycles and average concentrations of $C_{10}$ ($C_{10}$-nitrate + $C_{10}$-non-nitrate). Specifically, when adjusting a higher branching ratio of MT-b$RO_2$ radicals or autoxidation rate, the model captures the timing of peak concentrations of $C_{10}$-nitrate ($C_{10}$-ON), accurately although overestimates the average $C_{10}$-non-nitrate ($C_{10}$-NON) concentrations by approximately 50%. In contrast, when using lower branching ratio of MT-b$RO_2$ radicals or autoxidation rate, the model captures the values of $C_{10}$-NON relatively well but fails to agree with $C_{10}$-ON concentrations. These results highlight the need for further chamber experiments to accurately simulate the yields and reaction rates of different HOMs components.

The branching ratio of autoxidation-capable monoterpene radicals (MT-b$RO_2$) is the primary driver of uncertainties in HOMs formation, accounting for 19–41% of the variability in HOMs-SOA contributions to monoterpene-derived SOA. While autoxidation rates modulate radical lifetimes, their impact is secondary and dependent on MT-b$RO_2$ branching thresholds. This hierarchy of controls may help resolve long-standing discrepancies between chamber-derived parameterizations and global model predictions, , offering insights toward addressing a key gap identified in previous studies (Xu et al., 2022; Weber et al., 2021). The branching ratio of MT-b$RO_2$ mainly influences the formation of accretion products ($C_{15}$/$C_{20}$), which are dominated by cross-reactions between monoterpene- and isoprene-derived peroxy radicals, contributing approximately 50% of HOMs-SOA in pristine regions such as the Amazon. When the MT-b$RO_2$ branching ratio is higher, the concentrations of MT-HOM-$RO_2$ increase, resulting in more $C_{20}$ formed from MT-HOM-$RO_2$ self-reactions and more $C_{15}$ formed from ISOP-$RO_2$ + MT-HOM-$RO_2$ cross-reactions. This mechanism, underrepresented in earlier global models (Gordon et al., 2016; Zhu et al., 2019), highlights the competition between biogenic autoxidation and anthropogenic NO~~NOx~~-driven termination.

While $NO_x$ levels have minimal impact on total HOMs-SOA burdens, the formation pathways of $C_{10}$-ON and $C_{10}$-NON respond differently to NO~~NOx~~ variations. Increasing NO~~NOx~~ enhances $C_{10}$-ON production by promoting NO termination of MT-HOM-$RO_2$ radicals (e.g., 70% reduction in Centreville under the ~~LowNOx~~LowNO experiment), while simultaneously suppressing $HO_2$-driven $C_{10}$-NON formation. This is contrasts with the "NO~~NOx~~-oxidant-HOM" positive feedback

mechanism proposed by Pye et al. (2019). They demonstrated that although NO~~NOx~~ reduction increases the relative efficiency of autoxidation (enhancing $RO_2$ competition with NO), the concurrent decline in OH concentrations reduce the absolute HOM production rate. This leads to limited sensitivity of global HOMs-SOA burdens to NO~~NOx~~ variations. Our results show that while NO~~NOx~~ concentrations locally promote $C_{10}$-ON formation (e.g., in polluted regions), it simultaneously suppresses $C_{15}/C_{20}$ accretion product formation in pristine areas (e.g., the Amazon) by accelerating NO termination of MT-HOM-$RO_2$, inhibiting $RO_2$ autoxidation and cross-reactions. This leads to limited sensitivity of global HOMs-SOA burdens to NO~~NOx~~ variations. This mechanistic decoupling, , not fully emphasized in earlier nucleation-focused studies (e.g., Gordon et al., 2016), highlights the possible value of representing NO~~NOx~~ -HOMs interactions more explicitly in climate models.

The seasonal variation of HOMs-SOA is largely influenced by the intensity of biogenic emissions, with oxidant levels playing a secondary regulatory role. The background levels of NO, oxidant concentrations, and wet deposition conditions in different regions collectively shape the HOMs-SOA formation process. In high NO emission regions (such as the United States, Southeast Asian Continental Regions, Europe, and South Asia), $C_{10}$-ON predominates, while in low NO emission regions with high biogenic emissions (such as the Amazon rainforest and central Africa), the proportion of dimers ($C_{15}$ and $C_{20}$) is significantly increased.

This study investigates the formation of HOMs from monoterpene oxidation in a global simulation, yet significant uncertainties remain in the representation of $NO_3$-initiated pathways. Recent studies suggest that $NO_3$-initiated HOM formation may be more important than previously thought, particularly under polluted nighttime conditions. Chamber experiments on α- and β-phellandrene oxidation by $NO_3$ have shown significant SOA and HOM production, with SOA yields reaching approximately 35% and 60%, respectively, accompanied by abundant HOM monomers and dimers (Harb et al., 2024). Furthermore, field observations from the southeastern United States indicate that $NO_3$ remains the dominant oxidant of monoterpenes at night, accounting for around 60% (observed) to 80% (modeled) of total monoterpene oxidation (Desai et al., 2024). These results highlight the potential importance of $NO_3$-initiated HOM formation in contributing to organic aerosol formation under polluted nighttime conditions. However, due to structural differences in monoterpenes, such as ring strain and double-bond position, HOM yields vary widely among different species (Dam et al., 2022; Draper et al., 2024) and are highly sensitive to ambient $NO_x$ concentrations and humidity (Pasik et al., 2025; Li et al., 2022). The incomplete understanding of these mechanisms limits the accuracy of HOM predictions in models. Future research should combine field observations, laboratory constraints, and updated reaction schemes to reduce these uncertainties and improve global-scale modeling of nighttime organic aerosol formation.

Also, there may be some overestimations of $C_{15}$ and $C_{20}$ if all the accretion products are assumed to be ELVOC or ULVOC. In the updated model, $C_{15}H_{18}O_9$ ($C_{15}$, extremely low volatility) and $C_{20}H_{32}O_8$ ($C_{20}$, ultra-low volatility) are used as simplified representatives for all $C_{15}$ and $C_{20}$ dimers. While additional low-volatility dimer species have been detected in chamber

experiments (Stolzenburg et al., 2018; Ye et al., 2019; Schervish and Donahue, 2020), these studies did not provide explicit chemical kinetics for the reactions (i.e., intermediate products and their yields), which limits the ability to consider more precise volatility estimates for the accretion products in the model. This uncertainty may influence the contribution of both the accretion products and HOMs-SOA to the overall SOA.

In addition to volatility assumptions, uncertainties in the atmospheric removal processes of accretion products, particularly photolysis, may also affect their estimated concentrations. To assess the potential influence of photolysis uncertainties, we performed a sensitivity experiment assuming that accretion products photolyze at the same rate as particle-phase $C_{10}$ HOMs (i.e., 1.7% of the $NO_2$ photolysis rate). While the impact on smaller species such as $C_{10}$-ON and $C_{10}$-NON was negligible (<0.1%), substantial reductions were observed for $C_{15}$ and $C_{20}$ accretion products (75.2% and 68.1%, respectively) (Fig. S4). Overall, the total HOMs-SOA decreased by approximately 25.3% globally, highlighting that assumptions about photolysis rates can significantly affect model estimates of HOMs-SOA.

On a global scale, the formation of HOMs-SOA is influenced not only by chemical reaction mechanisms but also by their potential to indirectly affect radiative forcing through changes in cloud condensation nuclei (CCN). In particular, in tropical regions such as the Amazon and central Africa, where HOMs-SOA concentrations are high, the generated CCN could significantly influence the marine low cloud areas on the western side of continents. These changes in CCN may alter cloud droplet size and cloud reflectivity, thereby impacting the regional radiative balance.

Climate-driven increases in biogenic emissions may enhance HOMs-SOA production, but concurrent declines in anthropogenic NO~~NOx~~ could shift the dominant formation pathway from $C_{10}$-ON to $C_{10}$-NON, which is a feedback mechanism currently absent in projections. Additionally, aromatic-derived HOMs, which dominate nucleation and growth in polluted regions (Ren et al., 2021; Zhang et al., 2021; Shrivastava et al., 2024), remain underrepresented in global model. To address persistent gaps between model predictions and observations, field campaigns targeting accretion product speciation and chamber studies that constrain MT-b$RO_2$ branching ratios are needed.

**Competing interests.** At least one of the (co-)authors is a member of the editorial board of Atmospheric Chemistry and Physics.

**Data availability.** SENEX and BAECC field campaigns data are from (Xu et al., 2022).

SOAS campaign: https://csl.noaa.gov/groups/csl7/measurements/2013senex/Ground/DataDownload/

BAECC campaign: https://www.arm.gov/research/campaigns/amf2014baecc

SMEAR II dataset: https://smear.avaa.csc.fi/download

**Author contributions.** XD and MW designed the study. XS and YL performed the data analysis, produced the figures, and wrote the manuscript draft. RX, JT and MY collected the dataset. WS, MS, SA, and KS contributed to the analysis methods. DJ provided the model. All the authors contributed to discussion, writing, and editing of the manuscript.

**Acknowledgments.** This work is supported by the National Natural Science Foundation of China [grant numbers 2023YFE0121300, 2024YFC3711905, and 42361144711]. This research was also supported by Postgraduate Research and Practice Innovation Program of Jiangsu Province (KYCX25_0220), the Collaborative Innovation Center of Climate Change, Jiangsu Province, and supported by the Frontiers Science Center for Critical Earth Material Cycling. We greatly thank the High Performance Computing Center of Nanjing University for providing the computational resources used in this work. Manish Shrivastava was supported by the U.S. Department of Energy (DOE) Office of Science, Office of Biological and Environmental Research (BER) through the Early Career Research Program (Grant KP1701010/72144) and DOE BER's Atmospheric System Research (ASR) program (Grant KP1701010/57131). The Pacific Northwest National Laboratory (PNNL) is operated for DOE by Battelle Memorial Institute under contract DE-AC06-76RL01830. The CESM project is supported primarily by the United States National Science Foundation (NSF). This material is based upon work supported by the National Center for Atmospheric Research, which is a major facility sponsored by the NSF under Cooperative Agreement No. 1852977. We thank all the scientists, software engineers, and administrators who contributed to the development of CESM2.

## Reference


Baker, Y., Kang, S., Wang, H., Wu, R., Xu, J., Zanders, A., He, Q., Hohaus, T., Ziehm, T., Geretti, V., Bannan, T. J., O'Meara, S. P., Voliotis, A., Hallquist, M., McFiggans, G., Zorn, S. R., Wahner, A., and Mentel, T. F.: Impact of HO2/RO2 ratio on highly oxygenated α-pinene photooxidation products and secondary organic aerosol formation potential, Atmos. Chem. Phys., 24, 4789-4807, 10.5194/acp-24-4789-2024, 2024.

Beck, L. J., Schobesberger, S., Junninen, H., Lampilahti, J., Manninen, A., Dada, L., Leino, K., He, X.-C., Pullinen, I., Quéléver, L. L. J., Franck, A., Poutanen, P., Wimmer, D., Korhonen, F., Sipilä, M., Ehn, M., Worsnop, D. R., Kerminen, V.-M., Petäjä, T., Kulmala, M., and Duplissy, J.: Diurnal evolution of negative atmospheric ions above the boreal forest: from ground level to the free troposphere, Atmospheric Chemistry and Physics, 22, 8547-8577, 10.5194/acp-22-8547-2022, 2022.

Berndt, T., Scholz, W., Mentler, B., Fischer, L., Herrmann, H., Kulmala, M., and Hansel, A.: Accretion Product Formation from Self- and Cross-Reactions of RO2 Radicals in the Atmosphere, Angew Chem Int Ed Engl, 57, 3820-3824, 10.1002/anie.201710989, 2018.

Berndt, T., Richters, S., Jokinen, T., Hyttinen, N., Kurten, T., Otkjaer, R. V., Kjaergaard, H. G., Stratmann, F., Herrmann, H., Sipila, M., Kulmala, M., and Ehn, M.: Hydroxyl radical-induced formation of highly oxidized organic compounds, Nat Commun, 7, 13677, 10.1038/ncomms13677, 2016.

Bianchi, F., Kurten, T., Riva, M., Mohr, C., Rissanen, M. P., Roldin, P., Berndt, T., Crounse, J. D., Wennberg, P. O., Mentel, T. F., Wildt, J., Junninen, H., Jokinen, T., Kulmala, M., Worsnop, D. R., Thornton, J. A., Donahue, N., Kjaergaard, H. G., and Ehn, M.: Highly Oxygenated Organic Molecules (HOM) from Gas-Phase Autoxidation Involving Peroxy Radicals: A Key Contributor to Atmospheric Aerosol, Chem Rev, 119, 3472-3509, 10.1021/acs.chemrev.8b00395, 2019.

Carlton, A. G., de Gouw, J., Jimenez, J. L., Ambrose, J. L., Attwood, A. R., Brown, S., Baker, K. R., Brock, C., Cohen, R. C., Edgerton, S., Farkas, C. M., Farmer, D., Goldstein, A. H., Gratz, L., Guenther, A., Hunt, S., Jaeglé, L., Jaffe, D. A., Mak, J., McClure, C., Nenes, A., Nguyen, T. K., Pierce, J. R., de Sa, S., Selin, N. E., Shah, V., Shaw, S., Shepson, P. B., Song, S., Stutz, J., Surratt, J. D., Turpin, B. J., Warneke, C., Washenfelder, R. A., Wennberg, P. O., and Zhou, X.: Synthesis of the Southeast Atmosphere Studies: Investigating Fundamental Atmospheric Chemistry Questions, Bulletin of the American Meteorological Society, 99, 547-567, https://doi.org/10.1175/BAMS-D-16-0048.1, 2018.

Chung, S. H. and Seinfeld, J. H.: Global distribution and climate forcing of carbonaceous aerosols, Journal of Geophysical Research: Atmospheres, 107, AAC 14-11-AAC 14-33, https://doi.org/10.1029/2001JD001397, 2002.

Crounse, J. D., Nielsen, L. B., Jørgensen, S., Kjaergaard, H. G., and Wennberg, P. O.: Autoxidation of Organic Compounds in the Atmosphere, The Journal of Physical Chemistry Letters, 4, 3513-3520, 10.1021/jz4019207, 2013.

Dam, M., Draper, D. C., Marsavin, A., Fry, J. L., and Smith, J. N.: Observations of gas-phase products from the nitrate-radical-initiated oxidation of four monoterpenes, Atmos. Chem. Phys., 22, 9017-9031, 10.5194/acp-22-9017-2022, 2022.

Danabasoglu, G., Lamarque, J. F., Bacmeister, J., Bailey, D. A., DuVivier, A. K., Edwards, J., Emmons, L. K., Fasullo, J., Garcia, R., Gettelman, A., Hannay, C., Holland, M. M., Large, W. G., Lauritzen, P. H., Lawrence, D. M., Lenaerts, J. T. M., Lindsay, K., Lipscomb, W. H., Mills, M. J., Neale, R., Oleson, K. W., Otto-Bliesner, B., Phillips, A. S., Sacks, W., Tilmes, S., van Kampenhout, L., Vertenstein, M., Bertini, A., Dennis, J., Deser, C., Fischer, C., Fox-Kemper, B., Kay, J. E., Kinnison, D., Kushner, P. J., Larson, V. E., Long, M. C., Mickelson, S., Moore, J. K., Nienhouse, E., Polvani, L., Rasch, P. J., and Strand, W. G.: The Community Earth System Model Version 2 (CESM2), Journal of Advances in Modeling Earth Systems, 12, 10.1029/2019ms001916, 2020.

Desai, N. S., Moore, A. C., Mouat, A. P., Liang, Y., Xu, T., Takeuchi, M., Pye, H. O. T., Murphy, B., Bash, J., Pollack, I. B., Peischl, J., Ng, N. L., and Kaiser, J.: Impact of Heatwaves and Declining NOx on Nocturnal Monoterpene Oxidation in the Urban Southeastern United States, Journal of Geophysical Research: Atmospheres, 129, e2024JD041482, https://doi.org/10.1029/2024JD041482, 2024.

Donahue, N. M., Robinson, A. L., Stannier, C. O., and N., P. S.: Coupled partitioning, dilution, and chemical aging of semivolatile organics, Environ. Sci. Technol., 2006.

Draper, D., Almeida, T. G., Iyer, S., Smith, J. N., Kurtén, T., and Myllys, N.: Unpacking the diversity of monoterpene oxidation pathways via nitrooxy–alkyl radical ring-opening reactions and nitrooxy–alkoxyl radical bond scissions, Journal of Aerosol Science, 179, 106379, https://doi.org/10.1016/j.jaerosci.2024.106379, 2024.

Ehn, M., Thornton, J. A., Kleist, E., Sipila, M., Junninen, H., Pullinen, I., Springer, M., Rubach, F., Tillmann, R., Lee, B., Lopez-Hilfiker, F., Andres, S., Acir, I. H., Rissanen, M., Jokinen, T., Schobesberger, S., Kangasluoma, J., Kontkanen, J., Nieminen, T., Kurten, T., Nielsen, L. B., Jorgensen, S., Kjaergaard, H. G., Canagaratna, M., Dal Maso, M., Berndt, T., Petaja, T., Wahner, A., Kerminen, V. M., Kulmala, M.,

Worsnop, D. R., Wildt, J., and Mentel, T. F.: A large source of low-volatility secondary organic aerosol, Nature, 506, 476-+, 10.1038/nature13032, 2014a.

Ehn, M., Thornton, J. A., Kleist, E., Sipila, M., Junninen, H., Pullinen, I., Springer, M., Rubach, F., Tillmann, R., Lee, B., Lopez-Hilfiker, F., Andres, S., Acir, I. H., Rissanen, M., Jokinen, T., Schobesberger, S., Kangasluoma, J., Kontkanen, J., Nieminen, T., Kurten, T., Nielsen, L. B., Jorgensen, S., Kjaergaard, H. G., Canagaratna, M., Maso, M. D., Berndt, T., Petaja, T., Wahner, A., Kerminen, V. M., Kulmala, M., Worsnop, D. R., Wildt, J., and Mentel, T. F.: A large source of low-volatility secondary organic aerosol, Nature, 506, 476-479, 10.1038/nature13032, 2014b.

Emmons, L. K., Schwantes, R. H., Orlando, J. J., Tyndall, G., Kinnison, D., Lamarque, J. F., Marsh, D., Mills, M. J., Tilmes, S., Bardeen, C., Buchholz, R. R., Conley, A., Gettelman, A., Garcia, R., Simpson, I., Blake, D. R., Meinardi, S., and Pétron, G.: The Chemistry Mechanism in the Community Earth System Model Version 2 (CESM2), J. Adv. Model. Earth Sy., 12, 10.1029/2019ms001882, 2020.

Epstein, S. A., Riipinen, I., and Donahue, N. M.: A Semiempirical Correlation between Enthalpy of Vaporization and Saturation Concentration for Organic Aerosol, Environmental Science & Technology, 44, 743-748, 10.1021/es902497z, 2010.

Eyring, V., Bony, S., Meehl, G. A., Senior, C. A., Stevens, B., Stouffer, R. J., and Taylor, K. E.: Overview of the Coupled Model Intercomparison Project Phase 6 (CMIP6) experimental design and organization, Geosci. Model Dev., 9, 1937-1958, 10.5194/gmd-9-1937-2016, 2016.

Gelaro, R., McCarty, W., Suárez, M. J., Todling, R., Molod, A., Takacs, L., Randles, C. A., Darmenov, A., Bosilovich, M. G., Reichle, R., Wargan, K., Coy, L., Cullather, R., Draper, C., Akella, S., Buchard, V., Conaty, A., da Silva, A. M., Gu, W., Kim, G.-K., Koster, R., Lucchesi, R., Merkova, D., Nielsen, J. E., Partyka, G., Pawson, S., Putman, W., Rienecker, M., Schubert, S. D., Sienkiewicz, M., and Zhao, B.: The Modern-Era Retrospective Analysis for Research and Applications, Version 2 (MERRA-2), Journal of Climate, 30, 5419-5454, https://doi.org/10.1175/JCLI-D-16-0758.1, 2017.

Gordon, H., Sengupta, K., Rap, A., Duplissy, J., Frege, C., Williamson, C., Heinritzi, M., Simon, M., Yan, C., Almeida, J., Trostl, J., Nieminen, T., Ortega, I. K., Wagner, R., Dunne, E. M., Adamov, A., Amorim, A., Bernhammer, A. K., Bianchi, F., Breitenlechner, M., Brilke, S., Chen, X., Craven, J. S., Dias, A., Ehrhart, S., Fischer, L., Flagan, R. C., Franchin, A., Fuchs, C., Guida, R., Hakala, J., Hoyle, C. R., Jokinen, T., Junninen, H., Kangasluoma, J., Kim, J., Kirkby, J., Krapf, M., Kurten, A., Laaksonen, A., Lehtipalo, K., Makhmutov, V., Mathot, S., Molteni, U., Monks, S. A., Onnela, A., Perakyla, O., Piel, F., Petaja, T., Praplan, A. P., Pringle, K. J., Richards, N. A., Rissanen, M. P., Rondo, L., Sarnela, N., Schobesberger, S., Scott, C. E., Seinfeld, J. H., Sharma, S., Sipila, M., Steiner, G., Stozhkov, Y., Stratmann, F., Tome, A., Virtanen, A., Vogel, A. L., Wagner, A. C., Wagner, P. E., Weingartner, E., Wimmer, D., Winkler, P. M., Ye, P., Zhang, X., Hansel, A., Dommen, J., Donahue, N. M., Worsnop, D. R., Baltensperger, U., Kulmala, M., Curtius, J., and Carslaw, K. S.: Reduced anthropogenic aerosol radiative forcing caused by biogenic new particle formation, Proc Natl Acad Sci U S A, 113, 12053-12058, 10.1073/pnas.1602360113, 2016.

Guenther, A. B., Jiang, X., Heald, C. L., Sakulyanontvittaya, T., Duhl, T., Emmons, L. K., and Wang, X.: The Model of Emissions of Gases and Aerosols from Nature version 2.1 (MEGAN2.1): an extended and updated framework for modeling biogenic emissions, Geoscientific Model Development, 5, 1471-1492, 10.5194/gmd-5-1471-2012, 2012.

Harb, S., Cirtog, M., Alage, S., Cantrell, C., Cazaunau, M., Michoud, V., Pangui, E., Bergé, A., Giorio, C., Battaglia, F., and Picquet-Varrault, B.: HOMs and SOA formation from the oxidation of α- and β-phellandrenes by NO3 radicals, EGUsphere, 2024, 1-36, 10.5194/egusphere-2024-3419, 2024.

Henry, K. M. and Donahue, N. M.: Photochemical Aging of α-Pinene Secondary Organic Aerosol: Effects of OH Radical Sources and Photolysis, The Journal of Physical Chemistry A, 116, 5932-5940, 10.1021/jp210288s, 2012.

Hodzic, A., Kasibhatla, P. S., Jo, D. S., Cappa, C. D., Jimenez, J. L., Madronich, S., and Park, R. J.: Rethinking the global secondary organic aerosol (SOA) budget: stronger production, faster removal, shorter lifetime, Atmos. Chem. Phys., 16, 7917-7941, 10.5194/acp-16-7917-2016, 2016.

Jo, D. S., Hodzic, A., Emmons, L. K., Marais, E. A., Peng, Z., Nault, B. A., Hu, W., Campuzano-Jost, P., and Jimenez, J. L.: A simplified parameterization of isoprene-epoxydiol-derived secondary organic aerosol (IEPOX-SOA) for global chemistry and climate models: a case study with GEOS-Chem v11-02-rc, Geosci. Model Dev., 12, 2983-3000, 10.5194/gmd-12-2983-2019, 2019.

Jo, D. S., Hodzic, A., Emmons, L. K., Tilmes, S., Schwantes, R. H., Mills, M. J., Campuzano-Jost, P., Hu, W., Zaveri, R. A., Easter, R. C., Singh, B., Lu, Z., Schulz, C., Schneider, J., Shilling, J. E., Wisthaler, A., and Jimenez, J. L.: Future changes in isoprene-epoxydiol-derived secondary organic aerosol (IEPOX SOA) under the Shared Socioeconomic Pathways: the importance of physicochemical dependency, Atmos. Chem. Phys., 21, 3395-3425, 10.5194/acp-21-3395-2021, 2021.

Jokinen, T., Berndt, T., Makkonen, R., Kerminen, V. M., Junninen, H., Paasonen, P., Stratmann, F., Herrmann, H., Guenther, A. B., Worsnop, D. R., Kulmala, M., Ehn, M., and Sipila, M.: Production of extremely low volatile organic compounds from biogenic emissions: Measured yields and atmospheric implications, Proc Natl Acad Sci U S A, 112, 7123-7128, 10.1073/pnas.1423977112, 2015.

Kurten, T., Rissanen, M. P., Mackeprang, K., Thornton, J. A., Hyttinen, N., Jorgensen, S., Ehn, M., and Kjaergaard, H. G.: Computational Study of Hydrogen Shifts and Ring-Opening Mechanisms in alpha-Pinene Ozonolysis Products, J Phys Chem A, 119, 11366-11375, 10.1021/acs.jpca.5b08948, 2015.

Lee, B. H., Iyer, S., Kurtén, T., Varelas, J. G., Luo, J., Thomson, R. J., and Thornton, J. A.: Ring-opening yields and auto-oxidation rates of the resulting peroxy radicals from OH-oxidation of α-pinene and β-pinene, Environmental Science: Atmospheres, 3, 399-407, 10.1039/d2ea00133k, 2023.

Li, D., Huang, W., Wang, D., Wang, M., Thornton, J. A., Caudillo, L., Rörup, B., Marten, R., Scholz, W., Finkenzeller, H., Marie, G., Baltensperger, U., Bell, D. M., Brasseur, Z., Curtius, J., Dada, L., Duplissy, J., Gong, X., Hansel, A., He, X.-C., Hofbauer, V., Junninen, H., Krechmer, J. E., Kürten, A., Lamkaddam, H., Lehtipalo, K., Lopez, B., Ma, Y., Mahfouz, N. G. A., Manninen, H. E., Mentler, B., Perrier, S., Petäjä, T., Pfeifer, J., Philippov, M., Schervish, M., Schobesberger, S., Shen, J., Surdu, M., Tomaz, S., Volkamer, R., Wang, X., Weber, S. K., Welti, A., Worsnop, D. R., Wu, Y., Yan, C., Zauner-Wieczorek, M., Kulmala, M., Kirkby, J., Donahue, N. M., George, C., El-Haddad, I., Bianchi, F., and Riva, M.: Nitrate Radicals Suppress Biogenic New Particle Formation from Monoterpene Oxidation, Environmental Science & Technology, 58, 1601-1614, 10.1021/acs.est.3c07958, 2024.

Liu, X., Ma, P. L., Wang, H., Tilmes, S., Singh, B., Easter, R. C., Ghan, S. J., and Rasch, P. J.: Description and evaluation of a new four-mode version of the Modal Aerosol Module (MAM4) within version 5.3 of the Community Atmosphere Model, Geosci. Model Dev., 9, 505-522, 10.5194/gmd-9-505-2016, 2016.

Liu, Y., Dong, X., Wang, M., Emmons, L. K., Liu, Y., Liang, Y., Li, X., and Shrivastava, M.: Analysis of secondary organic aerosol simulation bias in the Community Earth System Model (CESM2.1), Atmos. Chem. Phys., 21, 8003-8021, 10.5194/acp-21-8003-2021, 2021.

Liu, Y., Dong, X., Emmons, L. K., Jo, D. S., Liu, Y., Shrivastava, M., Yue, M., Liang, Y., Song, Z., He, X., and Wang, M.: Exploring the Factors Controlling the Long-Term Trend (1988–2019) of Surface Organic Aerosols in the Continental United States by Simulations, J. Geophys. Res.-Atmos., 128, 10.1029/2022jd037935, 2023.

Lopez-Hilfiker, F. D., Mohr, C., Ehn, M., Rubach, F., Kleist, E., Wildt, J., Mentel, T. F., Lutz, A., Hallquist, M., Worsnop, D., and Thornton, J. A.: A novel method for online analysis of gas and particle composition: description and evaluation of a Filter Inlet for Gases and AEROsols (FIGAERO), Atmos. Meas. Tech., 7, 983-1001, 10.5194/amt-7-983-2014, 2014.

Mehra, A., Krechmer, J. E., Lambe, A., Sarkar, C., Williams, L., Khalaj, F., Guenther, A., Jayne, J., Coe, H., Worsnop, D., Faiola, C., and Canagaratna, M.: Oligomer and highly oxygenated organic molecule formation from oxidation of oxygenated monoterpenes emitted by California sage plants, Atmospheric Chemistry and Physics, 20, 10953-10965, 10.5194/acp-20-10953-2020, 2020.

Mohr, C., Thornton, J. A., Heitto, A., Lopez-Hilfiker, F. D., Lutz, A., Riipinen, I., Hong, J., Donahue, N. M., Hallquist, M., Petaja, T., Kulmala, M., and Yli-Juuti, T.: Molecular identification of organic vapors driving atmospheric nanoparticle growth, Nat.Commun., 10, 10.1038/s41467-019-12473-2, 2019.

Moller, K. H., Otkjaer, R. V., Chen, J., and Kjaergaard, H. G.: Double Bonds Are Key to Fast Unimolecular Reactivity in First-Generation Monoterpene Hydroxy Peroxy Radicals, J Phys Chem A, 124, 2885-2896, 10.1021/acs.jpca.0c01079, 2020.

Molteni, U., Simon, M., Heinritzi, M., Hoyle, C. R., Bernhammer, A.-K., Bianchi, F., Breitenlechner, M., Brilke, S., Dias, A., Duplissy, J., Frege, C., Gordon, H., Heyn, C., Jokinen, T., Kürten, A., Lehtipalo, K., Makhmutov, V., Petäjä, T., Pieber, S. M., Praplan, A. P., Schobesberger, S., Steiner, G., Stozhkov, Y., Tomé, A., Tröstl, J., Wagner, A. C., Wagner, R., Williamson, C., Yan, C., Baltensperger, U., Curtius, J., Donahue, N. M., Hansel, A., Kirkby, J., Kulmala, M., Worsnop, D. R., and Dommen, J.: Formation of Highly Oxygenated Organic Molecules from α-Pinene Ozonolysis: Chemical Characteristics, Mechanism, and Kinetic Model Development, ACS Earth and Space Chemistry, 3, 873-883, 10.1021/acsearthspacechem.9b00035, 2019.

Pankow, J. F.: An absorption model of the gas/aerosol partitioning involved in the formation of secondary organic aerosol, Atmospheric Environment, 28, 189-193, https://doi.org/10.1016/1352-2310(94)90094-9, 1994.

Pasik, D., Golin Almeida, T., Ahongshangbam, E., Iyer, S., and Myllys, N.: Monoterpene oxidation pathways initiated by acyl peroxy radical addition, Atmos. Chem. Phys., 25, 4313-4331, 10.5194/acp-25-4313-2025, 2025.

Petäjä, T., O'Connor, E. J., Moisseev, D., Sinclair, V. A., Manninen, A. J., Väänänen, R., von Lerber, A., Thornton, J. A., Nicoll, K., Petersen, W., Chandrasekar, V., Smith, J. N., Winkler, P. M., Krüger, O., Hakola, H., Timonen, H., Brus, D., Laurila, T., Asmi, E., Riekkola,

M.-L., Mona, L., Massoli, P., Engelmann, R., Komppula, M., Wang, J., Kuang, C., Bäck, J., Virtanen, A., Levula, J., Ritsche, M., and Hickmon, N.: BAECC: A Field Campaign to Elucidate the Impact of Biogenic Aerosols on Clouds and Climate, Bull. Amer. Meteor. Soc., 97, 1909-1928, https://doi.org/10.1175/BAMS-D-14-00199.1, 2016.

Piletic, I. R. and Kleindienst, T. E.: Rates and Yields of Unimolecular Reactions Producing Highly Oxidized Peroxy Radicals in the OH-Induced Autoxidation of alpha-Pinene, beta-Pinene, and Limonene, J Phys Chem A, 126, 88-100, 10.1021/acs.jpca.1c07961, 2022.

Praske, E., Otkjaer, R. V., Crounse, J. D., Hethcox, J. C., Stoltz, B. M., Kjaergaard, H. G., and Wennberg, P. O.: Atmospheric autoxidation is increasingly important in urban and suburban North America, Proc Natl Acad Sci U S A, 115, 64-69, 10.1073/pnas.1715540115, 2018.

Pye, H. O. T., D'Ambro, E. L., Lee, B. H., Schobesberger, S., Takeuchi, M., Zhao, Y., Lopez-Hilfiker, F., Liu, J., Shilling, J. E., Xing, J., Mathur, R., Middlebrook, A. M., Liao, J., Welti, A., Graus, M., Warneke, C., de Gouw, J. A., Holloway, J. S., Ryerson, T. B., Pollack, I. B., and Thornton, J. A.: Anthropogenic enhancements to production of highly oxygenated molecules from autoxidation, Proc Natl Acad Sci U S A, 116, 6641-6646, 10.1073/pnas.1810774116, 2019.

Ren, J., Chen, L., Fan, T., Liu, J., Jiang, S., and Zhang, F.: The NPF Effect on CCN Number Concentrations: A Review and Re-Evaluation of Observations From 35 Sites Worldwide, Geophysical Research Letters, 48, e2021GL095190, https://doi.org/10.1029/2021GL095190, 2021.

Richters, S., Herrmann, H., and Berndt, T.: Highly Oxidized RO2 Radicals and Consecutive Products from the Ozonolysis of Three Sesquiterpenes, Environ Sci Technol, 50, 2354-2362, 10.1021/acs.est.5b05321, 2016.

Robinson, A. L., Donahue, N. M., Shrivastava, M. K., Weitkamp, E. A., Sage, A. M., Grieshop, A. P., Lane, T. E., Pierce, J. R., and Pandis, S. N.: Rethinking Organic Aerosols: Semivolatile Emissions and Photochemical Aging, Science, 315, 1259, 10.1126/science.1133061, 2007.

Roldin, P., Ehn, M., Kurten, T., Olenius, T., Rissanen, M. P., Sarnela, N., Elm, J., Rantala, P., Hao, L., Hyttinen, N., Heikkinen, L., Worsnop, D. R., Pichelstorfer, L., Xavier, C., Clusius, P., Ostrom, E., Petaja, T., Kulmala, M., Vehkamaki, H., Virtanen, A., Riipinen, I., and Boy, M.: The role of highly oxygenated organic molecules in the Boreal aerosol-cloud-climate system, Nat Commun, 10, 4370, 10.1038/s41467-019-12338-8, 2019.

Rolletter, M., Kaminski, M., Acir, I. H., Bohn, B., Dorn, H. P., Li, X., Lutz, A., Nehr, S., Rohrer, F., Tillmann, R., Wegener, R., Hofzumahaus, A., Kiendler-Scharr, A., Wahner, A., and Fuchs, H.: Investigation of the α-pinene photooxidation by OH in the atmospheric simulation chamber SAPHIR, Atmos. Chem. Phys., 19, 11635-11649, 10.5194/acp-19-11635-2019, 2019.

Saunders, S. M., Jenkin, M. E., Derwent, R. G., and Pilling, M. J.: Protocol for the development of the Master Chemical Mechanism, MCM v3 (Part A): tropospheric degradation of non-aromatic volatile organic compounds, Atmos. Chem. Phys., 3, 161-180, 10.5194/acp-3-161-2003, 2003.

Schervish, M. and Donahue, N. M.: Peroxy radical chemistry and the volatility basis set, Atmospheric Chemistry and Physics, 20, 1183-1199, 10.5194/acp-20-1183-2020, 2020.

Shao, X., Wang, M., Dong, X., Liu, Y., Shen, W., Arnold, S. R., Regayre, L. A., Andreae, M. O., Pöhlker, M. L., Jo, D. S., Yue, M., and Carslaw, K. S.: Global modeling of aerosol nucleation with a semi-explicit chemical mechanism for highly oxygenated organic molecules (HOMs), Atmos. Chem. Phys., 24, 11365–11389, https://doi.org/10.5194/acp-24-11365-2024, 2024.

Shao, X., Wang, M., Dong, X., Liu, Y., Arnold, S. R., Regayre, L. A., Jo, D. S., Shen, W., Wang, H., Yue, M., Wang, J., Zhang, W., and Carslaw, K. S.: The effect of organic nucleation on the indirect radiative forcing with a semi-explicit chemical mechanism for highly oxygenated organic molecules (HOMs), EGUsphere [preprint], https://doi.org/10.5194/egusphere-2024-4135, 2025.

Shrivastava, M., Easter, R. C., Liu, X., Zelenyuk, A., Singh, B., Zhang, K., Ma, P.-L., Chand, D., Ghan, S., Jimenez, J. L., Zhang, Q., Fast, J., Rasch, P. J., and Tiitta, P.: Global transformation and fate of SOA: Implications of low-volatility SOA and gas-phase fragmentation reactions, Journal of Geophysical Research: Atmospheres, 120, 4169-4195, https://doi.org/10.1002/2014JD022563, 2015.

Shrivastava, M., Zhang, J., Zaveri, R. A., Zhao, B., Pierce, J. R., O'Donnell, S. E., Fast, J. D., Gaudet, B., Shilling, J. E., Zelenyuk, A., Murphy, B. N., Pye, H. O. T., Zhang, Q., Trousdell, J., and Chen, Q.: Anthropogenic Extremely Low Volatility Organics (ELVOCs) Govern the Growth of Molecular Clusters Over the Southern Great Plains During the Springtime, Journal of Geophysical Research: Atmospheres, 129, e2024JD041212, https://doi.org/10.1029/2024JD041212, 2024.

Stolzenburg, D., Fischer, L., Vogel, A. L., Heinritzi, M., Schervish, M., Simon, M., Wagner, A. C., Dada, L., Ahonen, L. R., Amorim, A., Baccarini, A., Bauer, P. S., Baumgartner, B., Bergen, A., Bianchi, F., Breitenlechner, M., Brilke, S., Buenrostro Mazon, S., Chen, D., Dias, A., Draper, D. C., Duplissy, J., El Haddad, I., Finkenzeller, H., Frege, C., Fuchs, C., Garmash, O., Gordon, H., He, X., Helm, J., Hofbauer, V., Hoyle, C. R., Kim, C., Kirkby, J., Kontkanen, J., Kürten, A., Lampilahti, J., Lawler, M., Lehtipalo, K., Leiminger, M., Mai, H., Mathot,

S., Mentler, B., Molteni, U., Nie, W., Nieminen, T., Nowak, J. B., Ojdanic, A., Onnela, A., Passananti, M., Petäjä, T., Quéléver, L. L. J., Rissanen, M. P., Sarnela, N., Schallhart, S., Tauber, C., Tomé, A., Wagner, R., Wang, M., Weitz, L., Wimmer, D., Xiao, M., Yan, C., Ye, P., Zha, Q., Baltensperger, U., Curtius, J., Dommen, J., Flagan, R. C., Kulmala, M., Smith, J. N., Worsnop, D. R., Hansel, A., Donahue, N. M., and Winkler, P. M.: Rapid growth of organic aerosol nanoparticles over a wide tropospheric temperature range, P. Natl. Acad. Sci. USA, 115, 9122-9127, 10.1073/pnas.1807604115, 2018.

Tilmes, S., Hodzic, A., Emmons, L. K., Mills, M. J., Gettelman, A., Kinnison, D. E., Park, M., Lamarque, J. F., Vitt, F., Shrivastava, M., Campuzano-Jost, P., Jimenez, J. L., and Liu, X.: Climate Forcing and Trends of Organic Aerosols in the Community Earth System Model (CESM2), Journal of Advances in Modeling Earth Systems, 11, 4323-4351, 10.1029/2019ms001827, 2019.

Tilmes, S., Lamarque, J. F., Emmons, L. K., Kinnison, D. E., Ma, P. L., Liu, X., Ghan, S., Bardeen, C., Arnold, S., Deeter, M., Vitt, F., Ryerson, T., Elkins, J. W., Moore, F., Spackman, J. R., and Val Martin, M.: Description and evaluation of tropospheric chemistry and aerosols in the Community Earth System Model (CESM1.2), Geoscientific Model Development, 8, 1395-1426, 10.5194/gmd-8-1395-2015, 2015.

Warneke, C., Trainer, M., de Gouw, J. A., Parrish, D. D., Fahey, D. W., Ravishankara, A. R., Middlebrook, A. M., Brock, C. A., Roberts, J. M., Brown, S. S., Neuman, J. A., Lerner, B. M., Lack, D., Law, D., Hubler, G., Pollack, I., Sjostedt, S., Ryerson, T. B., Gilman, J. B., Liao, J., Holloway, J., Peischl, J., Nowak, J. B., Aikin, K., Min, K. E., Washenfelder, R. A., Graus, M. G., Richardson, M., Markovic, M. Z., Wagner, N. L., Welti, A., Veres, P. R., Edwards, P., Schwarz, J. P., Gordon, T., Dube, W. P., McKeen, S., Brioude, J., Ahmadov, R., Bougiatioti, A., Lin, J. J., Nenes, A., Wolfe, G. M., Hanisco, T. F., Lee, B. H., Lopez-Hilfiker, F. D., Thornton, J. A., Keutsch, F. N., Kaiser, J., Mao, J., and Hatch, C.: Instrumentation and Measurement Strategy for the NOAA SENEX Aircraft Campaign as Part of the Southeast Atmosphere Study 2013, Atmos Meas Tech, 9, 3063-3093, 10.5194/amt-9-3063-2016, 2016.

Weber, J., Archer-Nicholls, S., Griffiths, P., Berndt, T., Jenkin, M., Gordon, H., Knote, C., and Archibald, A. T.: CRI-HOM: A novel chemical mechanism for simulating highly oxygenated organic molecules (HOMs) in global chemistry–aerosol–climate models, Atmos. Chem. Phys., 20, 10889-10910, 10.5194/acp-20-10889-2020, 2020a.

Weber, J., Archer-Nicholls, S., Griffiths, P., Berndt, T., Jenkin, M., Gordon, H., Knote, C., and Archibald, A. T.: CRI-HOM: A novel chemical mechanism for simulating highly oxygenated organic molecules (HOMs) in global chemistry–aerosol–climate models, Atmospheric Chemistry and Physics, 20, 10889-10910, 10.5194/acp-20-10889-2020, 2020b.

Weber, J., Archer-Nicholls, S., Abraham, N. L., Shin, Y. M., Bannan, T. J., Percival, C. J., Bacak, A., Artaxo, P., Jenkin, M., Khan, M. A. H., Shallcross, D. E., Schwantes, R. H., Williams, J., and Archibald, A. T.: Improvements to the representation of BVOC chemistry–climate interactions in UKCA (v11.5) with the CRI-Strat 2 mechanism: incorporation and evaluation, Geoscientific Model Development, 14, 5239-5268, 10.5194/gmd-14-5239-2021, 2021.

Xu, L., Moller, K. H., Crounse, J. D., Otkjaer, R. V., Kjaergaard, H. G., and Wennberg, P. O.: Unimolecular Reactions of Peroxy Radicals Formed in the Oxidation of alpha-Pinene and beta-Pinene by Hydroxyl Radicals, J Phys Chem A, 123, 1661-1674, 10.1021/acs.jpca.8b11726, 2019.

Ye, Q., Wang, M., Hofbauer, V., Stolzenburg, D., Chen, D., Schervish, M., Vogel, A., Mauldin, R. L., Baalbaki, R., Brilke, S., Dada, L., Dias, A., Duplissy, J., El Haddad, I., Finkenzeller, H., Fischer, L., He, X., Kim, C., Kürten, A., Lamkaddam, H., Lee, C. P., Lehtipalo, K., Leiminger, M., Manninen, H. E., Marten, R., Mentler, B., Partoll, E., Petäjä, T., Rissanen, M., Schobesberger, S., Schuchmann, S., Simon, M., Tham, Y. J., Vazquez-Pufleau, M., Wagner, A. C., Wang, Y., Wu, Y., Xiao, M., Baltensperger, U., Curtius, J., Flagan, R., Kirkby, J., Kulmala, M., Volkamer, R., Winkler, P. M., Worsnop, D., and Donahue, N. M.: Molecular Composition and Volatility of Nucleated Particles from α-Pinene Oxidation between −50 °C and +25 °C, Environ. Sci. Technol., 53, 12357-12365, 10.1021/acs.est.9b03265, 2019.

Zaveri, R. A., Easter, R. C., Singh, B., Wang, H., Lu, Z., Tilmes, S., Emmons, L. K., Vitt, F., Zhang, R., Liu, X., Ghan, S. J., and Rasch, P. J.: Development and Evaluation of Chemistry-Aerosol-Climate Model CAM5-Chem-MAM7-MOSAIC: Global Atmospheric Distribution and Radiative Effects of Nitrate Aerosol, J. Adv. Model. Earth. Syst., 13, 10.1029/2020ms002346, 2021.

Zawadowicz, M. A., Lee, B. H., Shrivastava, M., Zelenyuk, A., Zaveri, R. A., Flynn, C., Thornton, J. A., and Shilling, J. E.: Photolysis Controls Atmospheric Budgets of Biogenic Secondary Organic Aerosol, Environ. Sci. Technol., 54, 3861-3870, 10.1021/acs.est.9b07051, 2020.

Zhang, Q., Jia, S., Yang, L., Krishnan, P., Zhou, S., Shao, M., and Wang, X.: New particle formation (NPF) events in China urban clusters given by sever composite pollution background, Chemosphere, 262, 127842, https://doi.org/10.1016/j.chemosphere.2020.127842, 2021.

Zhao, B., Shrivastava, M., Donahue, N. M., Gordon, H., Schervish, M., Shilling, J. E., Zaveri, R. A., Wang, J., Andreae, M. O., Zhao, C., Gaudet, B., Liu, Y., Fan, J., and Fast, J. D.: High concentration of ultrafine particles in the Amazon free troposphere produced by organic new particle formation, Proc Natl Acad Sci U S A, 117, 25344-25351, 10.1073/pnas.2006716117, 2020.

Zhao, B., Donahue, N. M., Zhang, K., Mao, L., Shrivastava, M., Ma, P.-L., Shen, J., Wang, S., Sun, J., Gordon, H., Tang, S., Fast, J., Wang, M., Gao, Y., Yan, C., Singh, B., Li, Z., Huang, L., Lou, S., Lin, G., Wang, H., Jiang, J., Ding, A., Nie, W., Qi, X., Chi, X., and Wang, L.: Global variability in atmospheric new particle formation mechanisms, Nature, 631, 98-105, 10.1038/s41586-024-07547-1, 2024.

Zhao, Y., Thornton, J. A., and Pye, H. O. T.: Quantitative constraints on autoxidation and dimer formation from direct probing of monoterpene-derived peroxy radical chemistry, P. Natl. Acad. Sci. USA, 115, 12142-12147, 10.1073/pnas.1812147115, 2018.

Zhao, Y., Saleh, R., Saliba, G., Presto, A. A., Gordon, T. D., Drozd, G. T., Goldstein, A. H., Donahue, N. M., and Robinson, A. L.: Reducing secondary organic aerosol formation from gasoline vehicle exhaust, Proceedings of the National Academy of Sciences, 114, 6984-6989, doi:10.1073/pnas.1620911114, 2017.

Zhu, J., Penner, J. E., Yu, F., Sillman, S., Andreae, M. O., and Coe, H.: Decrease in radiative forcing by organic aerosol nucleation, climate, and land use change, Nat Commun, 10, 423, 10.1038/s41467-019-08407-7, 2019.